Science Advances
AAAS

FRONT MATTER

Title

Mechanochemically Accelerated Deconstruction of Chemically Recyclable Plastics

Authors

Mutian Hua[1], Zhengxing Peng[2], Rishabh D. Guha[3], Xiaoxu Ruan[3], Ka Chon Ng[4], Jeremy Demarteau[4], Shira Haber[1], Sophia N. Fricke[5], Jeffrey A. Reimer[5], Miquel B. Salmeron[1,4], Kristin A. Persson[1,3,4], Cheng Wang[2], Brett A. Helms[1,4,6*]

Affiliations

[1]Materials Sciences Division, Lawrence Berkeley National Laboratory; Berkeley CA, 94720 USA

[2]Advanced Light Source, Lawrence Berkeley National Laboratory; Berkeley CA, 94720 USA

[3]Department of Materials Sciences and Engineering, University of California Berkeley; Berkeley, CA 94720 USA

[4]The Molecular Foundry, Lawrence Berkeley National Laboratory; Berkeley CA, 94720 USA

[5]Department of Chemical and Biomolecular Engineering, University of California Berkeley; Berkeley, CA 94720 USA

[6]Chemical Sciences Division, Lawrence Berkeley National Laboratory; Berkeley CA, 94720 USA

*Corresponding author. Email: bahelms@lbl.gov

Abstract

Plastics redesign for circularity has primarily focused on monomer chemistries enabling faster deconstruction rates concomitant with high monomer yields. Yet, during deconstruction, polymer chains interact with their reaction medium, which remains underexplored in polymer reactivity. Here, we show that when plastics are deconstructed in reaction media that promote swelling, initial rates are accelerated by over 6-fold beyond that in small molecule analogues. This unexpected acceleration is primarily tied to mechanochemical activation of strained polymer chains, however, changes in the activity of water under polymer confinement and bond activation in solvent-separated ion pairs are also important. Taken together, deconstruction times can be shortened by 7 times by co-designing plastics and their deconstruction processes.

Teaser

Keys to unlocking faster plastics deconstruction rates at end of life are found in tailoring the reaction medium to control polymer mechanochemistry, solvation, and bond activation.

MAIN TEXT

Introduction

Closed-loop chemical recycling of plastic waste to reusable monomers can be undertaken with low carbon and energy intensity when mechanically recycled plastics are deconstructed as solids, suspended in a liquid reaction medium(*1–9*). During deconstruction, various species from the reaction medium partition into amorphous regions within the polymer, swelling the polymer and triggering chemical transformations therein. Yet, it remains a significant challenge to monitor and track reactions occurring in solvated polymer solids, leaving opaque the effects of polymer–solvent interactions on polymer reactivity.

Here, we show by using in-situ near-edge X-ray absorption fine structure (NEXAFS) and nuclear magnetic resonance (NMR) spectroscopic analysis that the rate of polymer deconstruction, thought to be dictated exclusively by monomer designs(*10–12*), is substantially higher when the polymer chains are stretched due to swelling in the reaction medium. Furthermore, by exploiting kosmotropic (stabilizing hydrogen bonding between water molecules) and chaotropic (disrupting hydrogen bonding between water molecules) counterions in the reaction medium to control the degree of swelling, we can modulate the extent of mechanochemical activation of cleavable bonds at the network level in circular plastics, increasing initial rates by six-fold. Concurrent with these effects, in-situ Raman spectroscopy studies and molecular dynamics simulations show that counterions further influence deconstruction rates at the molecular level by altering the structure of water near the sites of bond cleavage, which dictates the extent of bond activation toward hydrolysis. By understanding these combined effects across scales, we reveal compelling, non-obvious pathways for expediting polymer deconstruction: mechanochemical activation of hydrolysable bonds enables faster conversion of swollen polymer solids to dispersed

particulates in reactive liquid media, which should be explicitly tailored to maximize hydrolysis rates yielding reusable monomers in high yield through bond activation in smaller molecular fragments (**Fig. 1A**).

This understanding is a departure from conventional wisdom that might otherwise seek to explain polymer reactivity using theoretical insights or kinetic studies of small molecule models, which rarely consider the combined influence of heterogeneity, macromolecular architecture, chain conformation, solvation, and speciation(*10*, *11*, *13–15*). Furthermore, observations that mechanochemical activation of bonds in swollen polymers is important during the early stages of polymer deconstruction provide new lines of intrigue for mechanochemistry and its potential role in informing plastics redesign for circularity(*16–19*). We also find that the selection of reaction medium itself would benefit from the breadth of knowledge guiding the use of kosmotropic and chaotropic ions when seeking control over solvation(*20*, *21*), nucleation(*22–24*), crystallization(*25–27*), particularly in water-participating catalytic reactions(*28*, *29*). Doing so ensures that oligomer intermediates in chemical recycling of plastics can be more efficiently deconstructed to monomers at high rates and in high yield. This knowledge, when combined with information regarding the structure and activity of water alongside solvation-induced mechanochemical activation of polymer bonds, provides an unexpectedly clear vantage point that captures the underlying phenomena responsible for polymer deconstruction across scales and opens the door to new design concepts exploiting these behaviors in future plastics to enhance and ensure their recyclability.

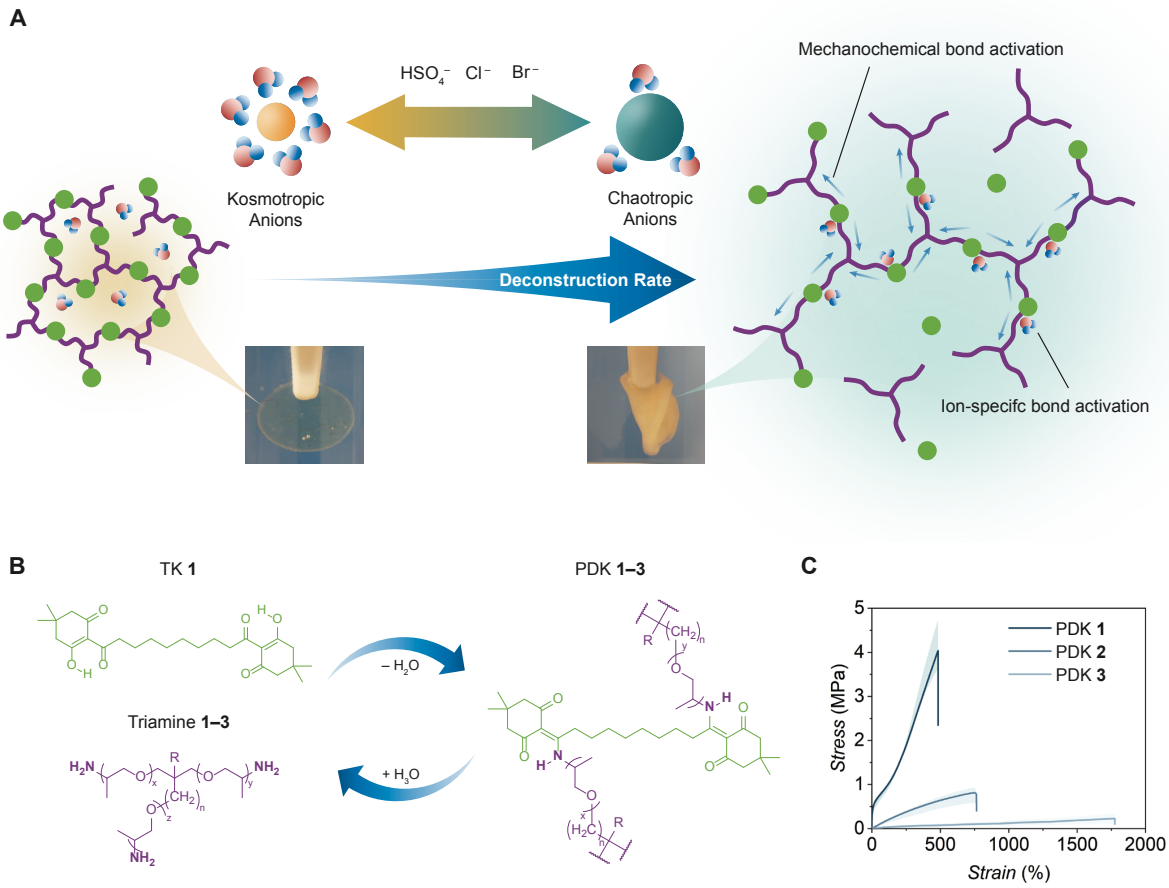

Fig.1. Enabling Circularity in Plastics by Accelerating Polymer Deconstruction Across Scales. (**A**) At early stages of heterogeneous polymer deconstruction, controlling the swelling of polymer chains is key to accelerating reaction rates for bond hydrolysis. At longer time scales, the structure of water near the remaining hydrolysable bonds in the dispersed solids dictates rates through hydrogen bond-mediated bond activation. The acid counterion plays distinct roles during each phase of deconstruction: the chaotropicity of the anion can be exploited to control swelling, while its ability to engage in hydrogen bonding with water affects the solvation environment near the bond undergoing hydrolysis. The inset photos showed the appearance of PDK elastomer discs clamped by a tweezer undergoing deconstruction in 5.0 M H_2SO_4 (left) and 5.0 M HBr (right) for 12 h under ambient temperature. (**B**) Chemical structure of TK **1** monomer (left green), triamine **1–3** (left

purple) monomer and the circular PDK elastomers (right). Triamine **1** is slightly different in its chemical structure compared to triamines **2–3**. *R* is hydrogen, and *n* is one for triamine **1.** *R* is an ethyl group, and *n* is zero for triamines **2** and **3**. (**C**) Tensile stress–strain curves of PDK elastomers **1**–**3**. Error bars were calculated as the standard deviation from the mean for three independently tested samples for each PDK formulation.

Results

Modular Platform for Controlling Polymer Swelling in Acidolytic Media

Polydiketoenamines (PDK) are an emerging family of highly recyclable polymers that are poised to replace several classes of difficult-to-recycle polymers, such as epoxy and polyurethane resins. Polydiketoenamines are synthesized from a diverse array of polytopic triketone and amine monomers via "click" polycondensation reactions(*8*). Segmental chain flexibility inherent to many polyetheramines enables the creation of polydiketoenamine elastomers that swell in acidolytic media, returning reusable monomers with high yield and purity(*30*). Lacking, however, has been a means to control the extent of PDK swelling in aqueous acid, which may depend on crosslinking density as well as the choice of acid.

To create PDK elastomers **1**–**3** with controlled crosslinking density, we combined a simple ditopic triketone monomer (TK **1**)(*8*) with either one of three tritopic amine-terminated polypropylene glycol crosslinkers (triamine **1–3**)(*31*), whose number-average molar masses were $M_n \sim 440$ g mol^{-1}, 3000 g mol^{-1}, and 5000 g mol^{-1}, respectively (**Fig. 1B & fig. S1–3**). PDK elastomers **1**–**3** therefrom were flexible with glass transition temperature (T_g) in the range of 17 to –60 °C and decomposition temperature (T_d) in the range of 272 to 328 °C (**fig. S4–5**). These elastomers exhibited a broad range of mechanical properties, including tensile strength up to 4.02 ± 0.68 MPa and tensile strain up to 1730 ± 350%, similar to

commercial epoxy resins as well as highly stretchable elastomers(*32*, *33*) (**Fig. 1C**). However, PDK elastomers **1**–**3** are distinctive from commercial materials in that they are thermally re-processible and chemically recyclable in a fully-closed loop (**fig. S6–7**)(*9*).

Mechanochemical Acceleration of Polymer Network Deconstruction

To differentiate the reactivity of polymers (**Fig. 2A**) from small molecules (**Fig. 2B**) during deconstruction, we carried out in-situ NEXAFS in an X-ray transparent liquid cell to monitor initial rates of acidolysis in solid PDK elastomers in contact with prescribed amount of an aqueous acid. Aqueous acid ionizes diketoenamine functionalities constituting the network, which in turn swells the polymer, in advance of hydrolysis reactions that ultimately generate triketone and triamine products. At ambient temperature, the hydrolysis reaction for this specific PDK network is slow, such that the X-ray set-up can be mounted without the PDK film experiencing significant chemical changes until triggered at the elevated temperature. The sensitivity of our methodology is dictated by the prevalence of spectroscopically distinctive chemical functionality in the reactants, intermediates, and products. Accordingly, we chose to study the effects of the reaction medium on deconstruction behaviors of elastomeric PDK **1**, owing to its higher concentration of diketoenamine bonds. To this end, we observed PDK **1** network deconstruction over 45 min at 60 °C, varying the acid as follows: 5.0 M H_2SO_4, 5.0 M HCl, and 5.0 M HBr (**Fig. 2C–E**). Prior to these experiments, we carried out extensive studies, modulating the incident X-ray flux to understand how best to minimize radiation damage to the sample as well as the volume of acid added to the in-situ cell to ensure signal-to-noise was adequate (**fig. S8**).

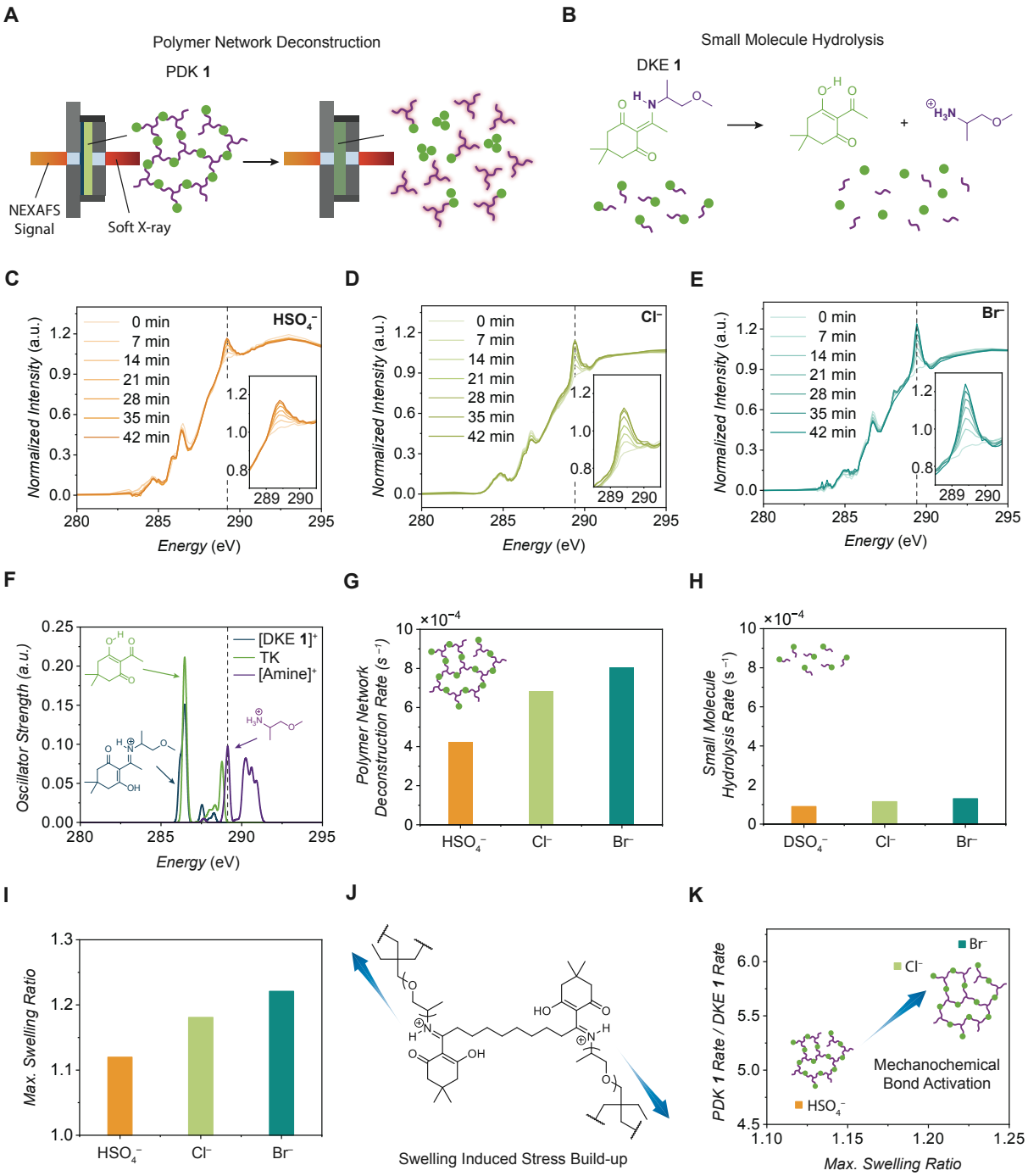

Fig. 2. Mechanochemical Activation of Hydrolysable Bonds in Solvated Polymer Networks. (**A**) Illustration of the deconstruction of PDK elastomers during in-situ NEXAFS measurements. (**B**) Illustration of the deconstruction of DKE **1**, a small molecule analogue of the hydrolysable bond in PDK elastomers. (**C**–**E**) Overlaid NEXAFS spectra of PDK **1** undergoing deconstruction in 5.0 M H_2SO_4, HCl and HBr at 60 °C. (**F**) TD-DFT simulated NEXAFS spectrum of protonated DKE **1**, and 2-Acetyl-5,5-dimethyl-1,3-cyclohexanedione

(TK), and 1-methoxy-2-propylamine, the acidolysis product of DKE **1**. (**G**) Deconstruction rates of PDK **1** in 5.0 M H_2SO_4, HCl and HBr at 60 °C. (**H**) Deconstruction rates of DKE **1** in 5.0 M D_2SO_4, DCl and DBr at 60 °C. (**I**) Maximum swelling ratio of PDK **1** during deconstruction in 5.0 M H_2SO_4, HCl and HBr at 60 °C. (**J**) Mechanochemical acceleration of diketoenamine acidolysis in solvated polymer networks. (**K**) Ratio of deconstruction rates at 60 °C for PDK **1** and DKE **1** as a function of PDK elastomer swelling ratio in different acidolytic media.

To interpret the data, we assigned features in the NEXAFS spectra by comparing them to simulated spectra for small molecule analogues of reactants, intermediates, and products by using time-dependent density function theory (TD-DFT)(*34*) (**Fig. 2F**, **fig. S9, 10**). We assigned the most prominent feature at 289.4 eV to C–N bonds exclusively present in liberated polyetheramine crosslinkers (i.e., acidolysis products), which enabled quantification of acidolysis rates. In contrast, less prominent features at 286.6 eV, corresponding to C=O bonds, were assignable to either diketoenamine moieties in PDK **1**–**3** (reactants) or liberated ß-triketones (products) and therefore less than ideal for precise quantification. To determine the initial rates of diketoenamine acidolysis, we thus calculated the peak areas at 289.4 eV and fit the data to a model for pseudo-first-order reaction kinetics (**fig. S11**). To our surprise, the initial rates for PDK deconstruction varied substantially by the composition of the acidolytic reaction medium: relative to the initial rate for PDK **1** deconstruction in 5.0 M H_2SO_4 ($-d[\mathrm{DKE}]/dt = 4.22 \times 10^{-4}$ s^{-1}), those for its deconstruction in 5.0 M HCl and HBr were 62% and 90% faster, respectively (**Fig. 2G**).

To clarify the origin of rate acceleration, we assessed by variable temperature ^{1}H NMR the initial rates of diketoenamine acidolysis for an analogous small molecule diketoenamine, DKE **1**, dissolved in each of the different acids. We conducted these studies at temperatures of 40 °C, 60 °C, and 80 °C, extracting the initial rates and then fit the data to a pseudo-first-order kinetics model (**Fig. 2H**, **fig. S12–14**). The initial rates of hydrolysis for DKE **1** at 60 °C showed similar trend as PDK **1** regarding anion type: relative to the initial rate for DKE **1** hydrolysis in 5.0 M D_2SO_4 ($-d$[DKE]/dt = 0.90 × 10^{-4} s^{-1}), those for DKE **1** hydrolysis in 5.0 M DCl and DBr were 27% and 44% faster, respectively. Yet most notably in all cases, the initial rates of PDK **1** deconstruction (**Fig. 2G**) were substantially higher than the rates for DKE **1** in a given acidolytic medium at a prescribed temperature (**Fig. 2H**), despite DKE **1** having more degrees of freedom as a dissolved solute than a diketoenamine bond would when part of a polymer network. In the presence of kosmotropic anions (HSO_4^-), the initial rate of PDK **1** deconstruction was 467% that of DKE **1**, and in the presence of chaotropic anions (Cl^-, Br^-), this ratio was increased to 596% and 616%. The high contrast of rates between PDK **1** and DKE **1**, and the relatively low contrast of rate between kosmotropic (HSO_4^-) and chaotropic anions (Cl^-, Br^-) suggested an acceleration mechanism that can be influenced by the type of anions but only present in a polymer network.

While the origin of this rate acceleration was not immediately clear, we observed differences in the degree of swelling depending on the acid type. Solvent up take in polymer networks leads to development of stress to balance the decrease in entropy *(16,17)*, thus higher degree of swelling generates higher stress in the polymer network. Connecting the trend of swelling and rate of polymer deconstruction could imply a mechanochemical effect introduced by the kosmotropic or chaotropic characters of the different acid anions (*20*, *35*). Consistent with this line of reasoning, the maximum swelling ratio increased in the order of HSO_4^-, Cl^-, and

Br^- (**Fig. 2I**, **fig. S15**). It is generally accepted that less-solvated chaotropic anions (Cl^-, Br^-) are driven to polymer–water interfaces, which in this case enhances swelling via more favorable solvation thermodynamics(*21*). Most notably, we found a strong positive correlation between the ratio of initial rates of diketoenamine bond hydrolysis in networked PDK **1** to those of small molecule DKE **1** in different acidolytic media as a function of the swelling ratio. Thus, solvation of polymer networks leads to pronounced mechanochemical activation of hydrolysable bonds as the major rate acceleration mechanism during early stages of polymer network deconstruction, regardless of the acid type; this effect is most pronounced in acidolytic media in which chaotropic anions collude with water to swell the network to the greatest extent (**Fig. 2J, K**).

Likewise noteworthy is the apparent influence of anion type on acidolysis rates for small molecules featuring a diketoenamine bond (i.e., DKE **1**) (**Fig. 2H**), which will gradually become the dominant factor for rate acceleration as the polymer network breaks down into smaller oligomers. The rate acceleration attained by changing acid anions was even more prominent when less thermal activation was provided. By decreasing the acidolysis temperature to 40 °C, the initial rates of DKE **1** hydrolysis in 5.0 M DCl and DBr were respectively 182% and 287% faster, than in 5.0 M D_2SO_4 (**fig. S12**), compared to a maximum of 44% attained at a temperature of 60 °C (**Fig. 2H**, **fig. S13**). This persistent rate acceleration tied directly to anions even in the absence of a strained polymer network necessitates further study into its acceleration mechanisms.

Understanding Bond Activation in Solvent-Separated Ion Pairs

To understand the apparent role of acid type on molecular diketoenamine hydrolysis rates (**Fig. 2H, fig. S12–14**), we considered the effects of solvation and ion-pairing as well as the activity of water and their relation to bond activation in the rate-limiting step, where water adds to an iminium intermediate along the reaction coordinate. It was clear from the standard free energies of activation ($\Delta G^{\ddagger}$) for DKE **1** hydrolysis—which were extracted from temperature-dependent ^{1}H NMR kinetics experiments (**Fig. 3A**, **fig. S16**)—that the energy landscape for diketoenamine hydrolysis was substantially altered in different acidolytic media. We carried out MD simulations of DKE **1** in those media (i.e., with explicit solvent and acid molecules) and revealed solvent-separated ion pairs, where a single water molecule was simultaneously bound to the iminium and any of the chaotropic halide ions through a series of hydrogen bonds (DKE **1** N–H···O, **Fig. 3B–D**). Furthermore, with increasing chaotropicity of the halide ions, we found that the number of hydrogen bonds between water molecules (Solvent H–O···H) was reduced (**Fig. 3B**), which is concomitant with an increase in the activity of water towards participating in hydrolysis reactions, owing to the greater availability of oxygen lone pair electrons. Concurrently, the residence time of water molecules at the reaction center was increased (**Fig. 3C**). The confluence of increased bond activation in solvent-separated ion pairs, higher water activity, and longer residence time near bonds undergoing hydrolysis produced improved kinetics as well as thermodynamics for acidolysis with increasing chaotropicity of the acid anions.

Supporting these simulations, we found by Raman spectroscopy of DKE **1** in 5.0 M acid solutions (**Fig. 3E**) that the ionization of the diketoenamine bond is evident in the blue shift of the feature at 1375 cm^{-1} (characterized in water) to 1403–1410 cm^{-1} (characterized in acids), which was assigned to the C=N bond. With increasing chaotropicity of the acid anion

(HSO_4^- < Cl^- < Br^- < I^-), the C=N bond was weakened, characterized by an increasing red-shift in the peak position relative to the same peak observed in the least chaotropic acid (HSO_4^-) and therefore was more susceptible towards hydrolysis (**Fig. 3F**). This is consistent with stronger hydrogen bonds in solvent-separated ion pairs, *i.e.*, anion–water–NH(iminium)(*36*, *37*) . We also observed changes in the structure and activity of water in the region of 3100–3700 cm^{-1}. The O–H stretching band in all samples was composed of two principal components: the first at ~3200 cm^{-1}, corresponding to tetrahedral water with four hydrogen bonds (4 H-bond H_2O); the second at ~3440 cm^{-1}, corresponding to water with two hydrogen bonds (2 H-bond H_2O)(*38*, *39*). With increasing chaotropicity of the anions, the tetrahedral structure of water was increasingly disrupted(*38*, *40*), as indicated by the diminution in the peak around 3200 cm^{-1}; the prevalence of higher-activity 2 H-bond H_2O features was increasingly dominant (**Fig. 3G**). This observation was further corroborated by Diffusion Ordered Spectroscopy (**table S1**) characterization of the same system, where increasing chaotropicity of the acid anion led to increased diffusivity of hydroniums in the reaction medium, as a result of the increased activity of water(*41*). Thus, stronger H-bonds in solvent-separated ion pairs weakens the hydrolysable iminium bond, activating it towards acidolysis, while the structure of water is re-organized to show higher activity, promoting acidolysis (**Fig. 3H**).

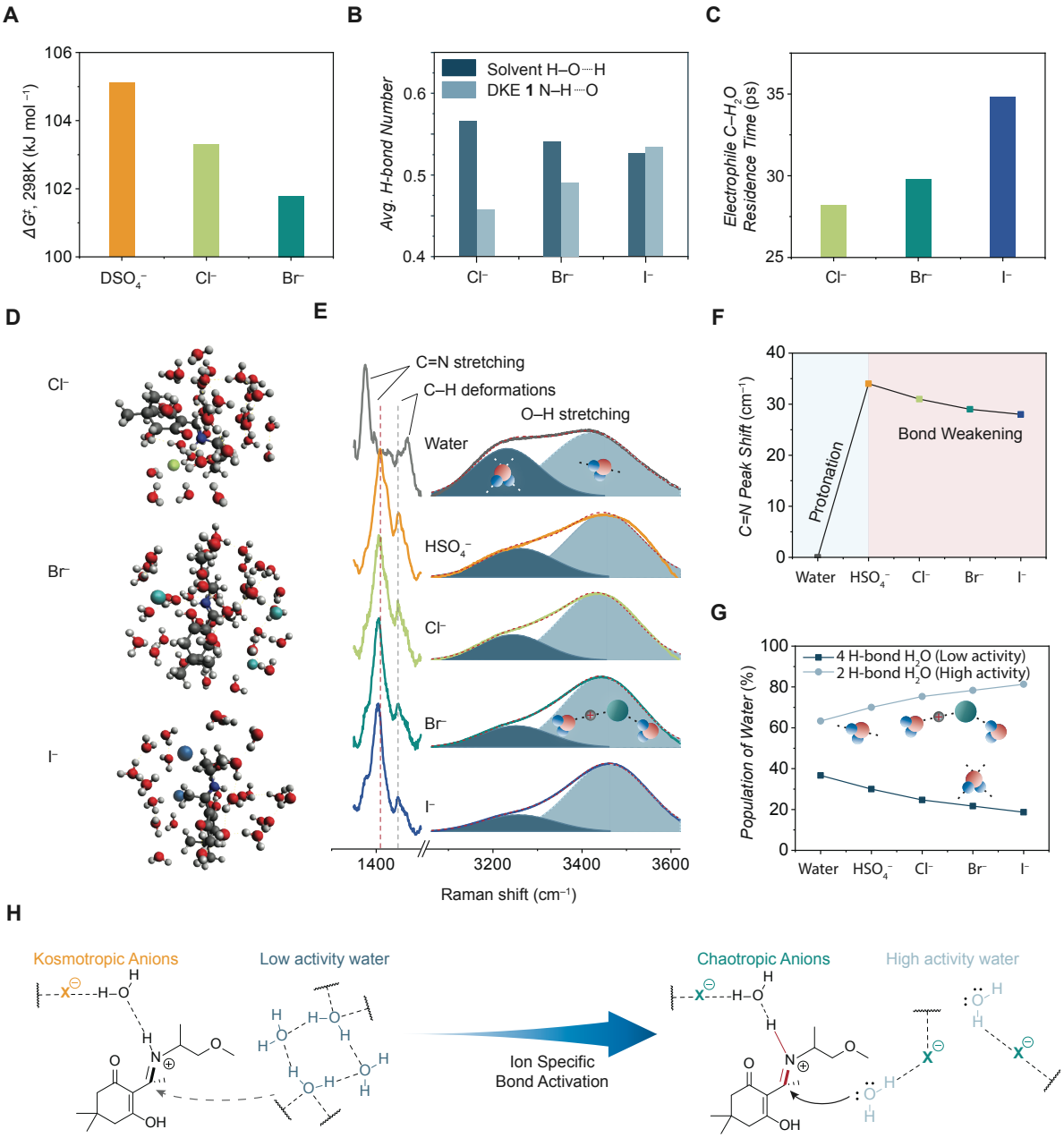

Fig. 3. Matched High Water Activity and Diketoenamine Bond Activation in Solvent-Separated Ion Pairs. (**A**) Experimentally determined $\Delta G^{\ddagger}$ for DKE **1** hydrolysis in 5.0 M D_2SO_4, DCl and DBr. (**B**) Average number of hydrogen bonds (H-bond) per water molecule in bulk solvent, per DKE **1** near the iminium obtained from molecular dynamics (MD) simulations. (**C**) Water residence time at the electrophile carbon of DKE **1** obtained from molecular dynamics (MD) simulations. (**D**) Snapshots of the MD simulations for DKE **1** in

different acidolytic media. (**E**) Raman spectra of DKE **1** in deionized water and 5.0 M H_2SO_4, HCl, HBr, and HI. Gaussian distributions are shown in blue for species of water with different hydrogen bonding configurations. The red dotted line is the fitted spectrum, combining the two Gaussians. (**F**) Shifts of C=N peak as a function of anion type. (**G**) Population of 4 H-bond water and 2 H-bond water as a function of anion type. (**H**) Illustration of bond activation due to the change in the structure of water. In the presence of chaotropic anions, stronger hydrogen bonds are formed between it, bound water, and the out-of-plane iminium species in solvent-separated ion pairs after the diketoenamine undergoes ionization in acid. Less hydrogen bonded water also exhibits higher activity during acidolysis.

Impacts of Accelerated Deconstruction Across Scales on Monomer Recovery

Understanding the implications of bond activation at the two length scales, we sought to control deconstruction of PDK elastomers by exploiting their interactions with the acidolytic reaction medium. At 60 °C, PDK **1** underwent deconstruction at different rates in 5.0 M HBr, HCl and H_2SO_4, which resulted in the progressive formation of smaller PDK solids (process 1) and ultimately colorless triketone precipitates (process 2) (**Fig. 4A**). While process 1 and 2 take place concurrently during PDK deconstruction, here we delineated the two processes for clarity of discussion. Processes 1 and 2 of PDK **1** deconstruction were fastest in 5.0 M HBr, where after only 1 h, triketone monomer had begun to precipitate from the reaction mixture; in 5.0 M HCl, this onset took 2 h; in 5.0 M H_2SO_4, 3 h was required. While we observed similar trends with acid composition for PDK **2** (**fig. S17**) and PDK **3** (**Fig. 4B**), it was notable that process 1 was slower overall for networks with lower crosslinking density. Therefore, polymer networks with low crosslinking density (and

concomitantly low volume fractions of ionizable functionality contributing to swelling) require tailored acidolytic media when it is desirable to accelerate their deconstruction via mechanochemical bond activation. For instance, the time to full disintegration of PDK **3** in 5.0 M H_2SO_4 and 5.0 M HCl was 7- and 3-times longer than that in 5.0 M HBr, respectively. Thus, the density of cleavable bonds within the network controls the rate at which bulk solids transform into smaller dispersed solids, allowing process 2 to proceed at rates dictated by surface area and the aforementioned polymer interactions with the acidolytic reaction medium vis-à-vis bond activation, water activity toward hydrolysis reactions, and water residence time near hydrolysable bonds.

In large reactors, where such transformations will eventually take place, stirring rates and residence times impact energy requirements for executing circularity at scale. The physical mechanisms described here are a means to tailor these to minimize such costs in the future, provided there are no discernable differences in the quality of recyclates produced by comparison to first-generation monomers. To verify this, we analyzed the purities and quantified the yields of TK **1** and triamine crosslinkers **1**–**3** recovered from deconstructed elastomeric PDK **1**–**3**, respectively, in each of the three acidolytic reaction media (**fig. S18**). In all cases, recovered TK **1** and triamine **1**–**3** were essentially indistinguishable from pristine monomers by ^{1}H NMR (**Fig. 4C**, **D**, **fig. S19–27**). The recovery yields were >90% with no obvious distinction between different acids. Thus, the interactions with polymers and acidolytic reaction media during polymer deconstruction can be tailored to more quickly generate higher surface area particulates that are easier to distribute within a reactor with stirring, such that subsequent monomer generation in the final stages of hydrolysis benefits from increased surface area. More specifically, the first process of network deconstruction

can be accelerated by mechanochemical effects tied to degree of swelling, while the second process can be accelerated by bond activation in solvent-separated ion pairs.

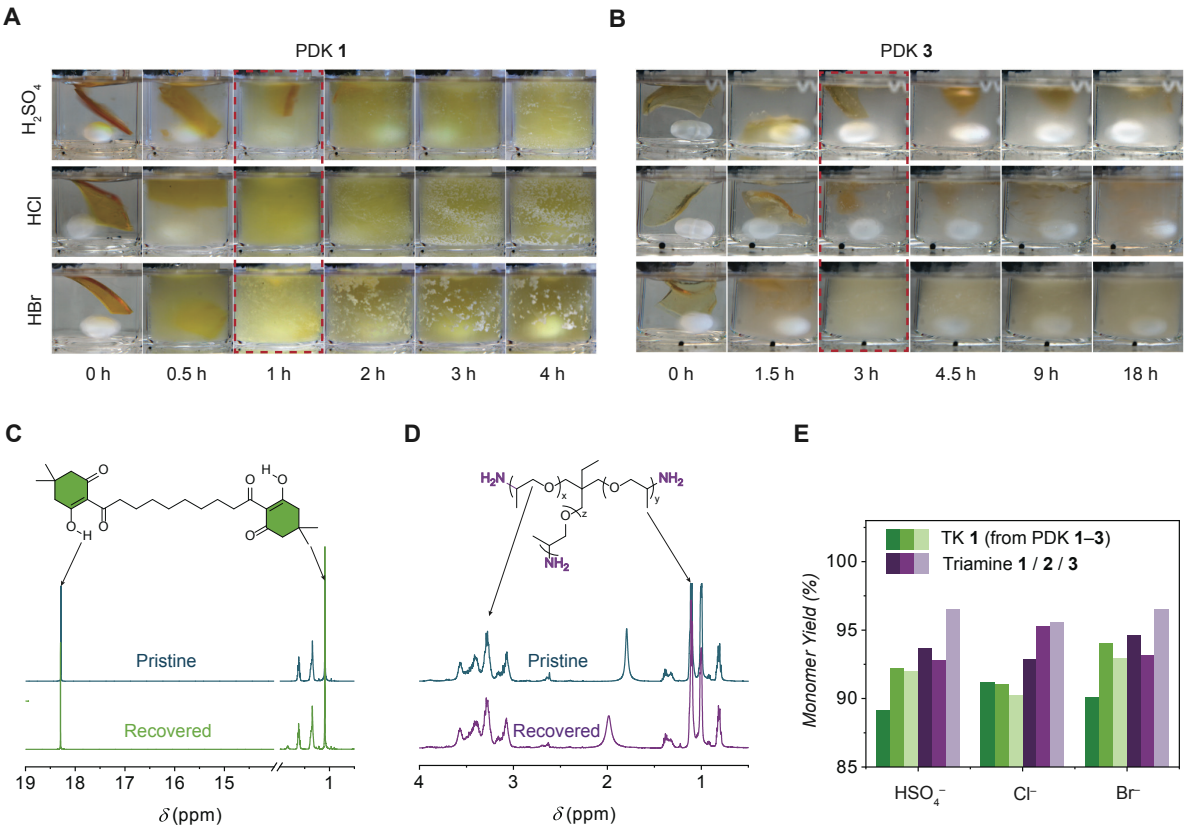

Fig. 4. Ion-Specific effects in PDK deconstruction in acid. (**A**) Snap-shots of PDK **1** undergoing acidolytic deconstruction in 5.0 M H_2SO_4, HCl, and HBr at 60 °C. (**B**) Snap-shots of PDK **3** undergoing acidolytic deconstruction in 5.0 M H_2SO_4, HCl, and HBr at 60 °C. (**C**) ^{1}H NMR spectrum of pristine (top) and recovered (bottom) TK **1** from PDK **1** deconstructed in 5.0 M HCl at 60 °C. (**D**) ^{1}H NMR spectrum of pristine (top) and recovered (bottom) triamine **1** from PDK **1** deconstructed in 5.0 M HCl at 60 °C. (**E**) Yields of recovered TK **1** and triamines **1**–**3** from PDK **1**–**3**, respectively, deconstructed in 5.0 M H_2SO_4, HCl and HBr at 60 °C.

Discussion

Deconstruction of polymer networks in acidolytic media reveals distinctive roles at different time and length scales played by network architecture and acid counterions. At early stages of deconstruction of macroscopic polymer solids, solvation and swelling of the network predominantly lead to an acceleration of deconstruction rates due to mechanochemical activation of hydrolysable bonds. Network swelling is enhanced for acid anions with increasing chaotropicity, resulting in initial rates that are more than 6-fold higher than those for small molecule analogues. As deconstruction proceeds, the influence of the reaction medium remains prominent due to the activation of hydrolysable bonds at the molecular scale, particularly in solvent-separated ion pairs; the activity of water also changes substantially with acid composition at high concentration, affecting rates in a manner which is matched to those of bond activation with different acid anions. These molecular-scale phenomena not only alter energy landscapes for bond hydrolysis ($\Delta\Delta G^{\ddagger}$ up to 3 kJ mol^{-1}), but also affect the water residence time near activated bonds and therefore the statistics of reactions producing reusable monomers. Thus, polymer–solvent interactions must be explicitly taken into account alongside monomer design when considering the fundamental and practical basis for recycling efficiency and circularity in plastics. Moreover, these interactions can now be accounted for by implementing workflows that combine synthetic chemistry, advanced in-situ characterization, and computational simulations at their relevant length and time scales.

Materials and Methods

Materials

5,5-dimethyl-1,3-cyclohexanedione (dimedone, 95%), *N*,*N*′-dicyclohexylcarbodiimide (DCC, 99%), 4-(dimethylamino)pyridine (DMAP, >99%), acetic acid (>99%), 2,5-dihydroxybenzoic acid (super DHB) were purchased from Sigma Aldrich and used as received. Sebacic acid (99%) was purchased from Arkema and used as received. Trimethylolpropane *tris*[poly(propylene glycol), amine terminated] ether (Triamine **1**, avg.

molar mass 440 g mol^{-1}) and propane-1,2,3-triol *tris*[poly(propylene glycol), amine terminated] ether (Triamine **2**, avg. molar mass 3000 g mol^{-1}; Triamine **3**, avg. molar mass 5000 g mol^{-1}) were obtained from Huntsman and used as received. 1-Methoxy-2-propylamine was purchased from ChemCruz and used as received. All solvents dichloromethane (DCM) (99%), tetrahydrofuran (THF) (99%), ethyl acetate (99%), methanol (99.8%) was purchased from VWR and used without further purification. All mineral acids was purchased from Sigma Aldrich and used without further purification. SiNx membranes with a square window were purchased from Norcada and used as received.

Methods

Nuclear Magnetic Resonance Spectroscopy.
^{1}H and ^{13}C Nuclear Magnetic Resonance Spectroscopy was carried out using a Bruker Avance II at 500 MHz. Chemical shifts are reported in δ (ppm) relative to the residual solvent peak: $CDCl_3$: 7.26 for ^{1}H. Splitting patterns are designated as s (singlet), d (doublet), t (triplet), q (quartet), and m (multiplet).

Fourier Transform Infrared Spectra (FTIR).
Data were acquired using Thermo-Fisher Nicolet iS50 spectrometer in Attenuated Total Reflectance (ATR) mode. Analytes were dissolved in THF, then drop casted on the diamond window and allowed to completely dry before starting the recording of spectrum.

Differential Scanning Calorimetry (DSC).
Data were acquired using a TA Instruments Q200 Differential Scanning Calorimeter. Samples were heated over a temperature range of 40–280 °C at a rate of 10 °C min^{-1} for the heating step and 50 °C min^{-1} for the cooling step under a N_2 atmosphere. For each sample, data acquisition runs consisted of a heating step, a cooling step, and a second heating step. Glass transition temperatures (T_g) were interpreted and reported from the second heating curve.

Thermogravimetric Analysis (TGA).
Thermogravimetric Analysis (TGA) was performed on a TA instruments TGA5500 Thermal Analyzer. First, samples were heated under nitrogen from 20 to 150 °C and hold at 150 °C for 60 min. Then, the samples were heated under nitrogen at a rate of 10 °C min^{-1} from 20 to 800 ºC. Mass loss and degradation temperatures were interpreted and reported from the second heating ramp.

Matrix-Assisted Laser Desorption/Ionization Time-of-Flight Mass Spectrometry (MALDI-ToF). MALDI mass spectra were recorded using a Bruker rapifleX spectrometer in positive reflector mode. A solution containing analyte (5 mg mL^{-1}), super DHB (20 mg mL^{-1}) was separately prepared in DCM and combined in 1:1 ratio before sample deposition. 1 µL of this mixture was applied to a stainless-steel target plate and allowed to dry completely before analysis.

Rheological Analysis.
Rheological characterizations including Amplitude sweep, frequency sweep, stress relaxation was carried out using a TA DHR-2 rheometer. PDK Elastomer samples were cut into 8 mm discs with a biopsy punch and loaded onto a rheometer between 8-mm stainless steel parallel plates.

Uniaxial Tensile testing.
Uniaxial Tensile measurements were carried out using an Instron 68TM-5 with 1 kN load cell at ambient temperature with a strain rate of 50 mm min^{-1}. Dog bone samples following ASTM D638 type V standard was cut using a stainless-steel die.

Near Edge X-ray Absorption Fine Structure (NEXAFS).
NEXAFS was caried out at the Advanced Light Source Beamline 11.0.1.2. The dry film and static liquid cell samples were mounted onto a controllable heating stage for temperature variation experiments.

Raman Spectroscopy.
Raman spectroscopy was performed using an Aramis Confocal Raman Microscope with incidence laser wavelength of 532 nm. The sample was dissolved in 5.0 M acid solution and dropped onto a glass slide for measurements.

Fabrication of PDK Elastomers.
Polydiketoenamine elastomers (PDK **1**–**3**) were synthesized by mixing the di-topic triketone monomer TK **1** and tri-topic amine monomer Triamines **1**–**3** separately in DCM using a vortex mixer followed by subsequent curing and solvent evaporation under 60 °C. The amine to triketone molar equivalence was kept at 1.3, and the solvent to total monomer weight ratio was kept at 1 for all formulations. Typically for the fabrication of PDK **1** elastomer, 1 g of TK **1** was first dissolved in 1 g of DCM and 0.94 g of triamine **1** was dissolved in 0.94 g DCM, the two solution was mixed in a scintillating vial. After stirring using a vortex mixer for 30 s, the solution became viscous and was poured into a PTFE mold. The subsequent curing of the elastomer and evaporation of the solvent was carried out at 60 °C overnight.

To reshape the PDK elastomers for subsequent characterization, the cured PDK elastomer was hot-pressed into sheets with thickness ~1 mm using a PTFE mold at 150 ˚C under 60 psi of pressure. Samples were cropped out of the PDK sheet into various shapes using stainless steel dies for uniaxial tensile testing, rheological measurements, and bulk depolymerization tests.

Fabrication of NEXAFS Samples.
Polydiketoenamine elastomers (PDK **1**) were spin-coated onto the SiNx windows from a dilute precursor solution with spin rate of 3000 rpm using a SCS 6800 Spin Coater. The precursor solution was prepared by dissolving 10 mg of di-topic triketone monomer TK **1** and 9.4 mg of tri-topic amine monomer triamine **1** in 1 g of THF.

For dry film samples, the PDK elastomer was spin coated onto a 5 × 5 mm SiNx window with a window size of 1.5 × 1.5 mm. The spin coated sample was thermally annealing at 60 °C for 2 h before used for testing.

For static liquid cell samples, the PDK elastomer was first spin coated onto a 7.5 × 7.5 mm frame SiNx window with a window size of 1 × 0.3 mm. The spin coated sample was then thermally annealing at 60 °C for 2 h to fully cure the elastomer. Subsequently, PDK elastomer thin film in the region outside of the window area was carefully removed using a razor blade. 0.3 μL of 5.0 M H_2SO_4 /HCl /HBr solution was then dropped onto the window area. Finally, another SiNx window with the frame dimension of 5 × 5 mm was carefully closed over the first window with the window area aligned, sandwiching the acid solution

and PDK thin film in the cell. Norland NOA68T epoxy was then applied over the edge of the second window, the epoxy was cured by irradiating with a handheld UV lamp for 2 min to create an airtight seal. The static liquid cell samples were immediately transferred into the testing chamber for characterization.

Acid-Catalyzed Hydrolytic Depolymerization of PDK Elastomers.
The hot-pressed PDK elastomers were cut into rectangular sheets with dimension around 10 (W) × 20 (H) × 1 (T) mm. The weight of each piece of PDK before depolymerization was recorded for subsequent yield calculations during recovery of the monomers. The PDK rectangle was immersed in 12 mL of 5.0 M H_2SO_4 / HCl / HBr in a 20 mL scintillating vial and allowed to depolymerize up to 96 h at 60 °C with gentle stirring.

*Recovery of TK 1 and Triamine **1**–**3** Monomers from PDK Elastomers.*
The mixture of depolymerized PDK was first cooled down to 4 °C and then filtered to separate the TK **1** precipitate and the triamine dissolved in acid solution.

To recover the triketone monomers, the retentate was first washed with the same type of acid used during depolymerization for 1 time and then washed with DI water for 2 times. The retentate was then dried under vacuum to yield an off-white solid. The crude recovered solid was then purified by recrystallizing in ethanol. The purity of the recovered TK **1** was verified by ^{1}H NMR. The recovery yield was calculated by dividing the weight of recovered TK **1** to the theoretical weight of TK **1** in the PDK sample used for depolymerization.

To recover the triamine monomers, the clear filtrate was first basified to pH 14 using 2.0 M KOH solutions. The filtrate turned slightly cloudy, with oily aggregates formed on the surface of the solution. The basified filtrate was then extracted using DCM. The organic phase was retained and dried under reduced pressure to yield a yellow viscous oil. The purity of the recovered triamine **1**–**3** was verified by ^{1}H NMR and MALDI-ToF. The recovery yield was calculated by comparing the weight of recovered triamine to the theoretical weight of triamine in the PDK sample used for depolymerization.

References

1. G. W. Coates, Y. D. Y. L. Getzler, Chemical recycling to monomer for an ideal, circular polymer economy. *Nat Rev Mater* **5**, 501–516 (2020).
2. B. A. Abel, R. L. Snyder, G. W. Coates, Chemically recyclable thermoplastics from reversible-deactivation polymerization of cyclic acetals. *Science (1979)* **373**, 783–789 (2021).
3. M. Häußler, M. Eck, D. Rothauer, S. Mecking, Closed-loop recycling of polyethylene-like materials. *Nature* **590**, 423–427 (2021).
4. D. Sathe, J. Zhou, H. Chen, H.-W. Su, W. Xie, T.-G. Hsu, B. R. Schrage, T. Smith, C. J. Ziegler, J. Wang, Olefin metathesis-based chemically recyclable polymers enabled by fused-ring monomers. *Nat Chem* **13**, 743–750 (2021).
5. L. Zhou, Z. Zhang, C. Shi, M. Scoti, D. K. Barange, R. R. Gowda, E. Y. X. Chen, Chemically circular, mechanically tough, and melt-processable polyhydroxyalkanoates. *Science* **380**, 64–69 (2023).
6. X. Wang, S. Zhan, Z. Lu, J. Li, X. Yang, Y. Qiao, Y. Men, J. Sun, X. Wang, S. Zhan, Z. Lu, J. Li, J. Sun, X. Yang, Y. Qiao, Y. Men, Healable, Recyclable, and

Mechanically Tough Polyurethane Elastomers with Exceptional Damage Tolerance. *Advanced Materials* **32**, 2005759 (2020).
7. L. P. Manker, G. R. Dick, A. Demongeot, M. A. Hedou, C. Rayroud, T. Rambert, M. J. Jones, I. Sulaeva, M. Vieli, Y. Leterrier, A. Potthast, F. Maréchal, V. Michaud, H.-A. Klok, J. S. Luterbacher, Sustainable polyesters via direct functionalization of lignocellulosic sugars. *Nat Chem* **14**, 976–984 (2022).
8. P. R. Christensen, A. M. Scheuermann, K. E. Loeffler, B. A. Helms, Closed-loop recycling of plastics enabled by dynamic covalent diketoenamine bonds. *Nat Chem* **11**, 442–448 (2019).
9. B. A. Helms, Polydiketoenamines for a Circular Plastics Economy. *Acc Chem Res* **55**, 2753–2765 (2022).
10. A. R. Epstein, J. Demarteau, B. A. Helms, K. A. Persson, Variable Amine Spacing Determines Depolymerization Rate in Polydiketoenamines. *J Am Chem Soc* **145**, 8089 (2023).
11. J. Demarteau, A. R. Epstein, P. R. Christensen, M. Abubekerov, H. Wang, S. J. Teat, T. J. Seguin, C. W. Chan, C. D. Scown, T. P. Russell, J. D. Keasling, K. A. Persson, B. A. Helms, Circularity in mixed-plastic chemical recycling enabled by variable rates of polydiketoenamine hydrolysis. *Sci Adv* **8**, 8823 (2022).
12. J. Demarteau, B. Cousineau, Z. Wang, B. Bose, S. Cheong, G. Lan, N. R. Baral, S. J. Teat, C. D. Scown, J. D. Keasling, B. A. Helms, Biorenewable and circular polydiketoenamine plastics. *Nat Sustain* **6**, 1426–1435 (2023).
13. J. B. Young, R. W. Hughes, A. M. Tamura, L. S. Bailey, K. A. Stewart, B. S. Sumerlin, Bulk depolymerization of poly(methyl methacrylate) via chain-end initiation for catalyst-free reversion to monomer. *Chem* **9**, 2669–2682 (2023).
14. L. D. Ellis, N. A. Rorrer, K. P. Sullivan, M. Otto, J. E. McGeehan, Y. Román-Leshkov, N. Wierckx, G. T. Beckham, Chemical and biological catalysis for plastics recycling and upcycling. *Nat Catal* **4**, 539–556 (2021).
15. M. Chu, Y. Liu, X. Lou, Q. Zhang, J. Chen, Rational Design of Chemical Catalysis for Plastic Recycling. *ACS Catal* **12**, 4659–4679 (2022).
16. F. K. Metze, S. Sant, Z. Meng, H. A. Klok, K. Kaur, Swelling-Activated, Soft Mechanochemistry in Polymer Materials. *Langmuir* **39**, 3546–3557 (2023).
17. C. K. Lee, C. E. Diesendruck, E. Lu, A. N. Pickett, P. A. May, J. S. Moore, P. V. Braun, Solvent swelling activation of a mechanophore in a polymer network. *Macromolecules* **47**, 2690–2694 (2014).
18. A. E. M. Beedle, M. Mora, C. T. Davis, A. P. Snijders, G. Stirnemann, S. Garcia-Manyes, Forcing the reversibility of a mechanochemical reaction. *Nat Commun* **9**, 3155 (2018).
19. J. Wang, X. Gao, A. Boarino, F. Célerse, C. Corminboeuf, H. A. Klok, Mechanical Acceleration of Ester Bond Hydrolysis in Polymers. *Macromolecules* **55**, 10145–10152 (2022).
20. Y. Zhang, S. Furyk, D. E. Bergbreiter, P. S. Cremer, Specific ion effects on the water solubility of macromolecules: PNIPAM and the Hofmeister series. *J Am Chem Soc* **127**, 14505–14510 (2005).
21. E. E. Bruce, N. F. A. Van Der Vegt, Molecular Scale Solvation in Complex Solutions. *J Am Chem Soc* **141**, 12948–12956 (2019).
22. Z. He, W. J. Xie, Z. Liu, G. Liu, Z. Wang, Y. Q. Gao, J. Wang, Tuning ice nucleation with counterions on polyelectrolyte brush surfaces. *Sci Adv* **2** (2016).
23. Q. Guo, Z. He, Y. Jin, S. Zhang, S. Wu, G. Bai, H. Xue, Z. Liu, S. Jin, L. Zhao, J. Wang, Tuning Ice Nucleation and Propagation with Counterions on Multilayer Hydrogels. *Langmuir* **34**, 11986–11991 (2018).

24. Z. He, C. Wu, M. Hua, S. Wu, D. Wu, X. Zhu, J. Wang, X. He, Bioinspired Multifunctional Anti-icing Hydrogel. *Matter* **2**, 723–734 (2020).
25. H. Zhang, W. Wang, S. Mallapragada, A. Travesset, D. Vaknin, Ion-Specific Interfacial Crystallization of Polymer-Grafted Nanoparticles. *Journal of Physical Chemistry C* **121**, 15424–15429 (2017).
26. S. Wu, C. Zhu, Z. He, H. Xue, Q. Fan, Y. Song, J. S. Francisco, X. C. Zeng, J. Wang, Ion-specific ice recrystallization provides a facile approach for the fabrication of porous materials. *Nat Commun* **8**, 15154 (2017).
27. M. Hua, S. Wu, Y. Ma, Y. Zhao, Z. Chen, I. Frenkel, J. Strzalka, H. Zhou, X. Zhu, X. He, Strong tough hydrogels via the synergy of freeze-casting and salting out. *Nature* **590**, 594–599 (2021).
28. J. Resasco, L. D. Chen, E. Clark, C. Tsai, C. Hahn, T. F. Jaramillo, K. Chan, A. T. Bell, Promoter Effects of Alkali Metal Cations on the Electrochemical Reduction of Carbon Dioxide. *J Am Chem Soc* **139**, 11277–11287 (2017).
29. H. Zhang, J. Gao, D. Raciti, A. S. Hall, Promoting Cu-catalysed CO2 electroreduction to multicarbon products by tuning the activity of H2O. *Nat Catal* **6**, 807–817 (2023).
30. E. A. Dailing, P. Khanal, A. R. Epstein, J. Demarteau, K. A. Persson, B. A. Helms, Circular Polydiketoenamine Elastomers with Exceptional Creep Resistance via Multivalent Cross-Linker Design. *ACS Cent Sci*, doi: 10.1021/acscentsci.3c01096 (2023).
31. Polyetheramines :: Huntsman Corporation (HUN). https://www.huntsman.com/products/detail/354/polyetheramines.
32. K. W. Harrison, D. Murtagh, H. Silva, J. G. Cordaro, Thermal Degradation Investigation of Polyurethane Elastomers using Thermal Gravimetric Analysis - Gas Chromatography/Mass Spectrometry. doi: 10.2172/1505419 (2017).
33. E. Darroman, N. Durand, B. Boutevin, S. Caillol, Improved cardanol derived epoxy coatings. *Prog Org Coat* **91**, 9–16 (2016).
34. J. Timoshenko, B. Roldan Cuenya, In Situ/ Operando Electrocatalyst Characterization by X-ray Absorption Spectroscopy. *Chem Rev* **121**, 882–961 (2021).
35. X. Chen, T. Yang, S. Kataoka, P. S. Cremer, Specific ion effects on interfacial water structure near macromolecules. *J Am Chem Soc* **129**, 12272–12279 (2007).
36. N. Ghosh, S. Roy, A. Bandyopadhyay, J. A. Mondal, Vibrational Raman Spectroscopy of the Hydration Shell of Ions. *Liquids* **3**, 19–39 (2022).
37. J. L. Fulton, M. Balasubramanian, Structure of hydronium (H3o+)/chloride (Cl -) contact ion pairs in aqueous hydrochloric acid solution: A zundel-like local configuration. *J Am Chem Soc* **132**, 12597–12604 (2010).
38. Q. Sun, The Raman OH stretching bands of liquid water. *Vib Spectrosc* **51**, 213–217 (2009).
39. Y.-H. Wang, S. Zheng, W.-M. Yang, R.-Y. Zhou, Q.-F. He, P. Radjenovic, J.-C. Dong, S. Li, J. Zheng, Z.-L. Yang, G. Attard, F. Pan, Z.-Q. Tian, J.-F. Li, In situ Raman spectroscopy reveals the structure and dissociation of interfacial water. *Nature* **600**, 81–85 (2021).
40. M. Ahmed, V. Namboodiri, A. K. Singh, J. A. Mondal, S. K. Sarkar, How ions affect the structure of water: A combined raman spectroscopy and multivariate curve resolution study. *Journal of Physical Chemistry B* **117**, 16479–16485 (2013).
41. M. J. Blandamer, J. B. F. N. Engberts, P. T. Gleeson, J. C. R. Reis, Activity of water in aqueous systems; A frequently neglected property. *Chem Soc Rev* **34**, 440–458 (2005).

42. X. Man, M. Doi, Swelling Dynamics of a Disk-Shaped Gel. Macromolecules 54(10), 4626-4632 (2021)
43. S. Hirata, M. Head-Gordon, Time-dependent density functional theory within the Tamm–Dancoff approximation. *Chem Phys Lett* **314**, 291–299 (1999).
44. R. L. Gieseking, M. A. Ratner, G. C. Schatz, Semiempirical modeling of Ag nanoclusters: New parameters for optical property studies enable determination of double excitation contributions to plasmonic excitation. *Journal of Physical Chemistry A* **120**, 4542–4549 (2016).
45. E. Epifanovsky, A. T. B. Gilbert, X. Feng, J. Lee, Y. Mao, N. Mardirossian, P. Pokhilko, A. F. White, M. P. Coons, A. L. Dempwolff, Z. Gan, D. Hait, P. R. Horn, L. D. Jacobson, I. Kaliman, J. Kussmann, A. W. Lange, K. U. Lao, D. S. Levine, J. Liu, S. C. McKenzie, A. F. Morrison, K. D. Nanda, F. Plasser, D. R. Rehn, M. L. Vidal, Z. Q. You, Y. Zhu, B. Alam, B. J. Albrecht, A. Aldossary, E. Alguire, J. H. Andersen, V. Athavale, D. Barton, K. Begam, A. Behn, N. Bellonzi, Y. A. Bernard, E. J. Berquist, H. G. A. Burton, A. Carreras, K. Carter-Fenk, R. Chakraborty, A. D. Chien, K. D. Closser, V. Cofer-Shabica, S. Dasgupta, M. De Wergifosse, J. Deng, M. Diedenhofen, H. Do, S. Ehlert, P. T. Fang, S. Fatehi, Q. Feng, T. Friedhoff, J. Gayvert, Q. Ge, G. Gidofalvi, M. Goldey, J. Gomes, C. E. González-Espinoza, S. Gulania, A. O. Gunina, M. W. D. Hanson-Heine, P. H. P. Harbach, A. Hauser, M. F. Herbst, M. Hernández Vera, M. Hodecker, Z. C. Holden, S. Houck, X. Huang, K. Hui, B. C. Huynh, M. Ivanov, Á. Jász, H. Ji, H. Jiang, B. Kaduk, S. Kähler, K. Khistyaev, J. Kim, G. Kis, P. Klunzinger, Z. Koczor-Benda, J. H. Koh, D. Kosenkov, L. Koulias, T. Kowalczyk, C. M. Krauter, K. Kue, A. Kunitsa, T. Kus, I. Ladjánszki, A. Landau, K. V. Lawler, D. Lefrancois, S. Lehtola, R. R. Li, Y. P. Li, J. Liang, M. Liebenthal, H. H. Lin, Y. S. Lin, F. Liu, K. Y. Liu, M. Loipersberger, A. Luenser, A. Manjanath, P. Manohar, E. Mansoor, S. F. Manzer, S. P. Mao, A. V. Marenich, T. Markovich, S. Mason, S. A. Maurer, P. F. McLaughlin, M. F. S. J. Menger, J. M. Mewes, S. A. Mewes, P. Morgante, J. W. Mullinax, K. J. Oosterbaan, G. Paran, A. C. Paul, S. K. Paul, F. Pavošević, Z. Pei, S. Prager, E. I. Proynov, Á. Rák, E. Ramos-Cordoba, B. Rana, A. E. Rask, A. Rettig, R. M. Richard, F. Rob, E. Rossomme, T. Scheele, M. Scheurer, M. Schneider, N. Sergueev, S. M. Sharada, W. Skomorowski, D. W. Small, C. J. Stein, Y. C. Su, E. J. Sundstrom, Z. Tao, J. Thirman, G. J. Tornai, T. Tsuchimochi, N. M. Tubman, S. P. Veccham, O. Vydrov, J. Wenzel, J. Witte, A. Yamada, K. Yao, S. Yeganeh, S. R. Yost, A. Zech, I. Y. Zhang, X. Zhang, Y. Zhang, D. Zuev, A. Aspuru-Guzik, A. T. Bell, N. A. Besley, K. B. Bravaya, B. R. Brooks, D. Casanova, J. Da Chai, S. Coriani, C. J. Cramer, G. Cserey, A. E. Deprince, R. A. Distasio, A. Dreuw, B. D. Dunietz, T. R. Furlani, W. A. Goddard, S. Hammes-Schiffer, T. Head-Gordon, W. J. Hehre, C. P. Hsu, T. C. Jagau, Y. Jung, A. Klamt, J. Kong, D. S. Lambrecht, W. Liang, N. J. Mayhall, C. W. McCurdy, J. B. Neaton, C. Ochsenfeld, J. A. Parkhill, R. Peverati, V. A. Rassolov, Y. Shao, L. V. Slipchenko, T. Stauch, R. P. Steele, J. E. Subotnik, A. J. W. Thom, A. Tkatchenko, D. G. Truhlar, T. Van Voorhis, T. A. Wesolowski, K. B. Whaley, H. L. Woodcock, P. M. Zimmerman, S. Faraji, P. M. W. Gill, M. Head-Gordon, J. M. Herbert, A. I. Krylov, Software for the frontiers of quantum chemistry: An overview of developments in the Q-Chem 5 package. *Journal of Chemical Physics* **155**, 84801 (2021).
46. N. A. Besley, M. J. G. Peach, D. J. Tozer, Time-dependent density functional theory calculations of near-edge X-ray absorption fine structure with short-range corrected functionals. *Physical Chemistry Chemical Physics* **11**, 10350–10358 (2009).

47. E. D. Glendening, D. Feller, Cation-water interactions. The M+(H2O)n clusters for alkali metals, M = Li, Na, K, Rb, and Cs. *Journal of physical chemistry* **99**, 3060–3067 (1995).
48. P. Eastman, M. S. Friedrichs, J. D. Chodera, R. J. Radmer, C. M. Bruns, J. P. Ku, K. A. Beauchamp, T. J. Lane, L. P. Wang, D. Shukla, T. Tye, M. Houston, T. Stich, C. Klein, M. R. Shirts, V. S. Pande, OpenMM 4: A Reusable, Extensible, Hardware Independent Library for High Performance Molecular Simulation. *J Chem Theory Comput* **9**, 461–469 (2013).
49. GitHub - orionarcher/pymatgen-io-openmm: A Pymatgen IO module for setting up OpenMM simulations. https://github.com/orionarcher/pymatgen-io-openmm.
50. S. Boothroyd, P. K. Behara, O. C. Madin, D. F. Hahn, H. Jang, V. Gapsys, J. R. Wagner, J. T. Horton, D. L. Dotson, M. W. Thompson, J. Maat, T. Gokey, L. P. Wang, D. J. Cole, M. K. Gilson, J. D. Chodera, C. I. Bayly, M. R. Shirts, D. L. Mobley, Development and Benchmarking of Open Force Field 2.0.0: The Sage Small Molecule Force Field. *J Chem Theory Comput* **19**, 3251 (2023).
51. W. L. Jorgensen, J. Chandrasekhar, J. D. Madura, R. W. Impey, M. L. Klein, Comparison of simple potential functions for simulating liquid water. *J Chem Phys* **79**, 926–935 (1983).
52. T. A. Halgren, Performance of MMFF94*. *Scope, Parameterization, and Journal of Computational Chemistry* **17**, 490–519 (1996).
53. B. J. Kirby, P. Jungwirth, Charge Scaling Manifesto: A Way of Reconciling the Inherently Macroscopic and Microscopic Natures of Molecular Simulations. *J Phys Chem Lett* **10**, 7531–7536 (2019).
54. D. C. Liu, J. Nocedal, On the limited memory BFGS method for large scale optimization. *Math Program* **45**, 503–528 (1989).
55. Z. Zhang, X. Liu, K. Yan, M. E. Tuckerman, J. Liu, Unified Efficient Thermostat Scheme for the Canonical Ensemble with Holonomic or Isokinetic Constraints via Molecular Dynamics. *J Phys Chem A* **123**, 6056–6079 (2019).
56. R. J. Gowers, M. Linke, J. Barnoud, T. J. E. Reddy, M. N. Melo, S. L. Seyler, J. Domanski, D. L. Dotson, S. Buchoux, I. M. Kenney, O. Beckstein, MDAnalysis: A Python Package for the Rapid Analysis of Molecular Dynamics Simulations. *Proceedings of the 15th Python in Science Conference*, 98–105 (2019).
57. O. A. Cohen, H. Macdermott-Opeskin, L. Lee, T. Hou, K. D. Fong, R. Kingsbury, J. Wang, K. A. Persson, SolvationAnalysis: A Python toolkit for understanding liquid solvation structure in classical molecular dynamics simulations. *J Open Source Softw* **8**, 5183 (2023).

Acknowledgments

Funding: This work was funded by the U.S. Department of Energy, Office of Science, Office of Basic Energy Sciences, Materials Sciences and Engineering Division under contract no. DE-AC02-05-CH11231, Unlocking Chemical Circularity in Recycling by Controlling Polymer Reactivity across Scales program CUP-LBL-Helms.

Work at the Molecular Foundry—including polymer synthesis, characterization, X-ray liquid cell assembly, Raman spectroscopy characterization—was supported by the Office of Science, Office of Basic Energy Sciences, of the U.S. Department of Energy under Contract No. DE-AC02-05CH11231.

Work at the Advanced Light Source—including NEXAFS—was supported by the Office of Science, Office of Basic Energy Sciences, of the U.S. Department of Energy under the same contract.

This research used the Savio computational cluster resource provided by the Berkeley Research Computing program at the University of California, Berkeley (supported by the UC Berkeley chancellor, vice chancellor for research, and chief information officer).

The instrument used in this work for the pulsed field gradient NMR (diffusion ordered spectroscopy) is supported by the National Science Foundation under Grant No. 2018784.

Author contributions: B.A.H contributed to the conceptualization of the project. B.A.H and M.H. contributed to the design of the project. B.A.H and J.D. contributed to the design of the PDK elastomer. M.H., Z.P and C.W. contributed to the design, experiment, and data analysis of NEXAFS characterization. R.D.G. contributed to the TD-DFT simulations of NEXAFS spectra. X.R. contributed to the MD simulations. M.H and K.C.N contributed to the experiment and data analysis of Raman spectroscopy. M.H., S.H., and S.N.F. contributed to the NMR characterization and analysis. B.A.H. and M.H. contributed to visualization. B.A.H. and M.H. wrote the original draft. All authors contributed to the final draft and editing. B.A.H, C.W., K.A.P., M.B.S., J.A.R. supervised research, provided project administration, and acquired funding. We thank Norman Su and Huntsman Corp. for providing the triamine monomers used in the study.

Competing interests: B.A.H. is an inventor on the U.S. provisional patent application 62/587,148 and submitted by Lawrence Berkeley National Laboratory that covers PDKs, as well as aspects of their use and recovery. J.D., K.A.P., and B.A.H. are inventors on the U.S. provisional patent application 63/390,962 submitted by Lawrence Berkeley National Laboratory that covers elastomeric PDKs, as well as aspects of their use and recovery. B.A.H. has a financial interest in Cyklos Materials and Sepion Technologies. The authors declare that they have no other competing interests.

Data and materials availability: The data that support the findings of this study are available from the corresponding author upon reasonable request.

Supplementary Materials

Supplementary Text

Figs. S1 to S27

Tables S1 to S5

References (*42–57*)

Science Advances
AAAS

Supplementary Materials for

Mechanochemically Accelerated Deconstruction of Chemically Recyclable Plastics

Mutian Hua, Zhengxing Peng, Rishabh D. Guha, Xiaoxu Ruan, Ka Chon Ng, Jeremy Demarteau, Shira Haber, Sophia N. Fricke, Jeffrey A. Reimer, Miquel B. Salmeron, Kristin A. Persson, Cheng Wang, Brett A. Helms*

Corresponding author: bahelms@lbl.gov

The PDF file includes:

Supplementary Text

Synthetic Methods

*Synthesis of Ditopic Triketone Monomer, TK **1**.*

1,10-bis(2-hydroxy-4,4-dimethyl-6-oxocyclohex-1-en-1-yl)decane-1,10-dione (TK **1)**, was synthesized as previously described[8]. Briefly, dimedone (20.0 g, 0.143 mol), sebacic acid (13.7 g, 0.068 mol), DMAP (24.9 g, 0.204 mol) was dissolved in dichloromethane (100 mL) in a round bottom flask. To the mixture solution, a separate solution of DCC (33.7 g, 0.163 mol) in dichloromethane (80 mL) was added dropwise at room temperature, and the reaction was allowed to proceed for 24 h. The resulting solution was first filtered to remove dicyclohexylurea, and the organic phase was washed three times with 1.0 M HCl solution to remove DMAP. The organic phase was then concentrated under reduced pressure to obtain a yellow-orange solid. The crude product was then dissolved in 200 mL of 2.0 M KOH and washed three times with dichloromethane. The aqueous phase was acidified with 2.0 M HCl to precipitate an off-white solid. The solid was collected by filtration and dried under reduced pressure. ^{1}H NMR analysis of the product was consistent with the previous report (see below). ^{1}H NMR (500 MHz, $CDCl_3$): δ 18.30(s, 2H), 3.03 (br s, 4H), 2.55 (s, 4H), 2.38 (s, 4H), 1.62 (br s, 4H), 1.35 (br s, 8H), 1.10 (s, 12H) ppm.

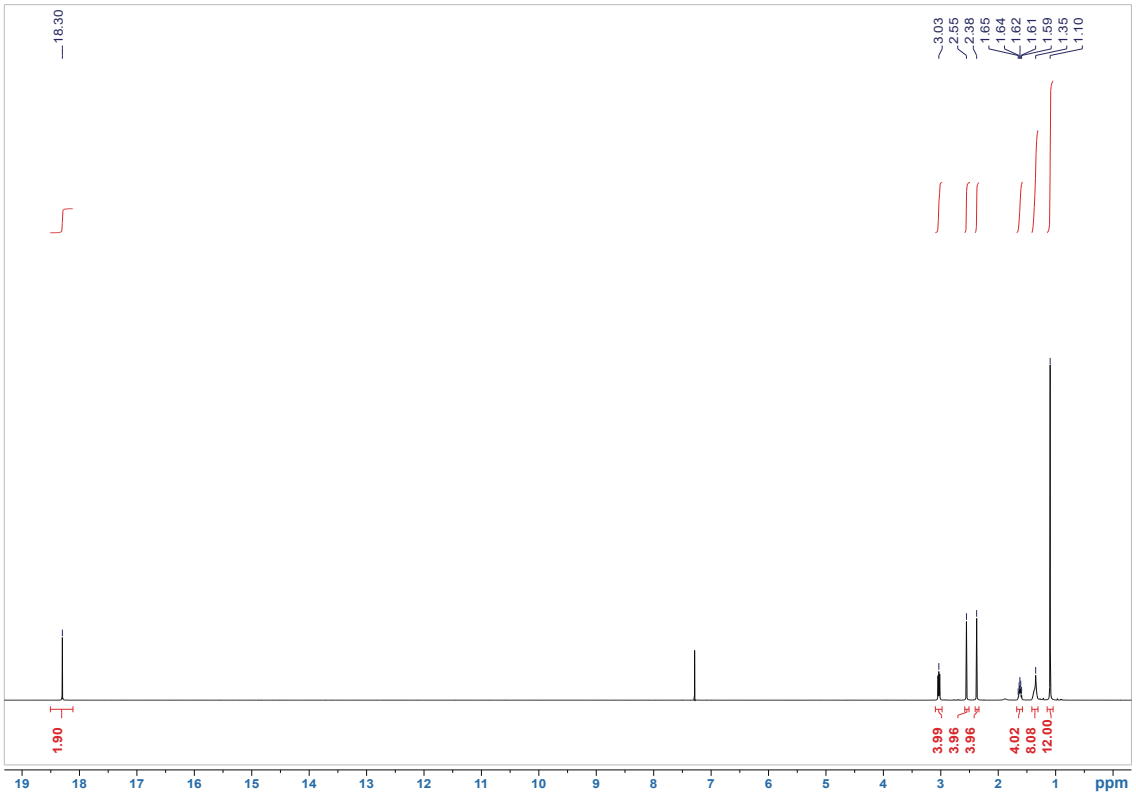

Synthesis of Monotopic Triketone Monomer, 2-Acetyl-5,5-dimethyl-1,3-cyclohexanedione.

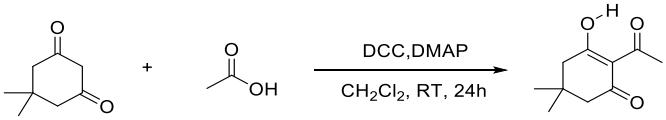

The monotopic triketone monomer, 2-Acetyl-5,5-dimethyl-1,3-cyclohexanedione, was synthesized as previously described8. Briefly, dimedone (5.0 g, 0.0357 mol), acetic acid (13.7 g, 0.068 mol), DMAP (5.9 g, 0.0486 mol) was dissolved in dichloromethane (20 mL) in a round bottom flask. To the mixture solution, a separate solution of DCC (8.0 g, 0.0389 mol) in dichloromethane (20 mL) was added dropwise at room temperature, and the reaction was allowed to proceed for 24 h. The resulting solution was first filtered to remove dicyclohexylurea, and the organic phase was washed three times with 1.0 M HCl solution to remove DMAP. The product was extracted from the organic phase using 100 mL of 2.0 M KOH solution for two times. The aqueous phase was combined and acidified with 250 mL of 2.0 M HCl solution to yield a cloudy solution. The product was extracted using with 100 mL of DCM. The organic phase was dried over $MgSO_4$ and concentrated under reduced pressure to obtain a white crystalline solid. ^{1}H NMR analysis of the product was consistent with the previous report (see below). ^{1}H NMR (500 MHz, CDCl3) δ 18.16 (s, 1H), 2.63 (s, 3H), 2.55 (s, 2H), 2.38 (s, 2H), 1.10 (s, 6H) ppm.

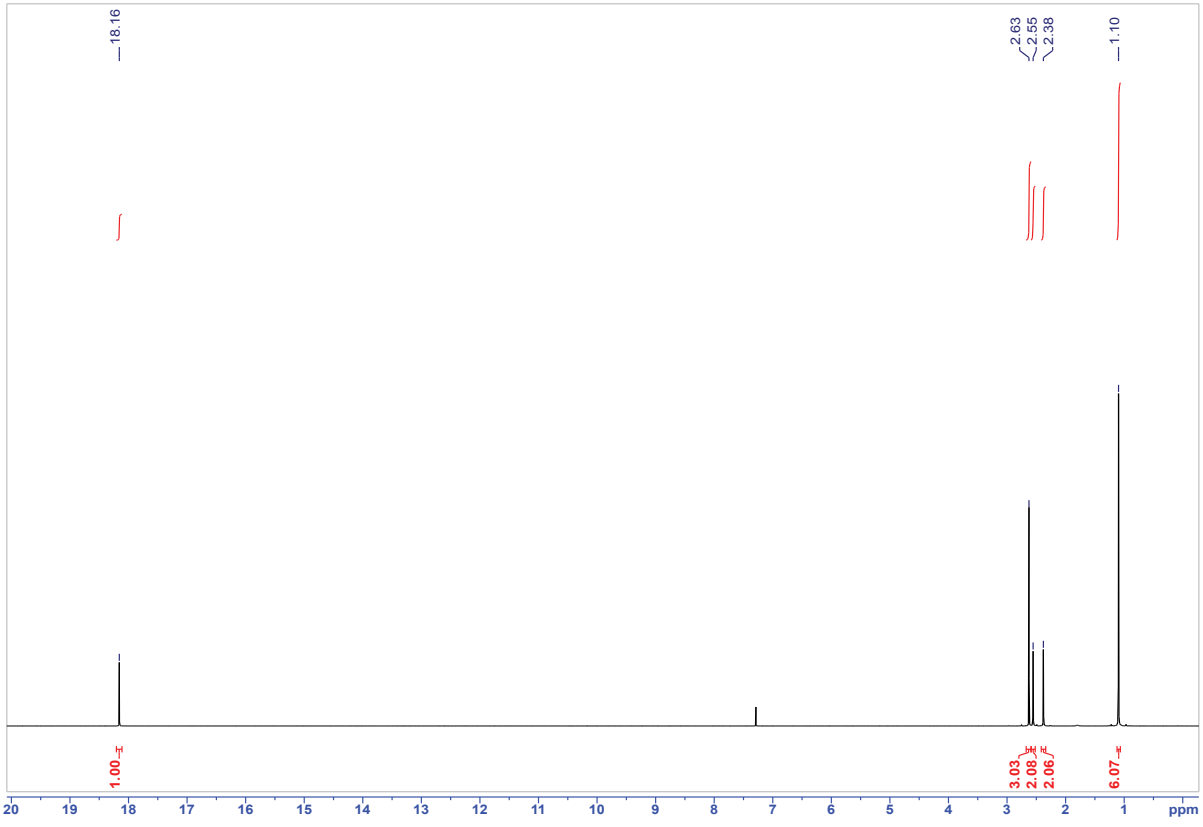

*Synthesis of diketoenamine small molecule, DKE **1***

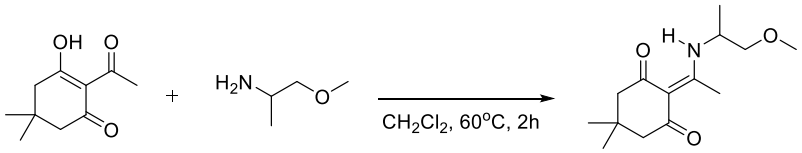

Briefly, 2-Acetyl-5,5-dimethyl-1,3-cyclohexanedione (0.50 g, 2.75 mmol), 1-Methoxy-2-propylamine (0.24 g, 2.75 mmol) was dissolved in dichloromethane (3 mL) in a 4 mL glass vial. The mixture solution was heated to 60 ˚C, and the reaction was allowed to proceed for 2 h with gentle stirring. The product was purified by column chromatography using EtOAc as the eluent (SiO2, 100% EtOAc). Column fractions containing pure product were combined and solvent was removed under reduced pressure to yield an off-white solid (84% isolated yield). ^{1}H NMR, C^{13} NMR and FT-IR analysis of the product is as below. ^{1}H NMR (500MHz, $CDCl_3$): δ 13.62 (s, 1H), 4.04 (br s, 1H), 3.41-3.49 (m, 2H), 3.40 (s, 3H), 2.60 (s, 3H), 2.39 (s, 4H), 1.30 (d, 3H), 1.04 (s, 6H) ppm; ^{13}C NMR(125MHz, $CDCl_3$), δ 197.97, 172.92, 107.77, 75.72, 59.39, 52.84, 49.20, 30.14, 28.30, 18.21, 17.97 ppm. FT-IR: 3521, 3176, 1636, 1565, 1456, 1422, 1384, 1366, 1324, 1299, 1286, 1199, 1171, 1140, 1106, 1051, 1024, 974, 954, 927, 906, 819, 728, 666, 627, 582, 550, 463 cm $^{-1}$.

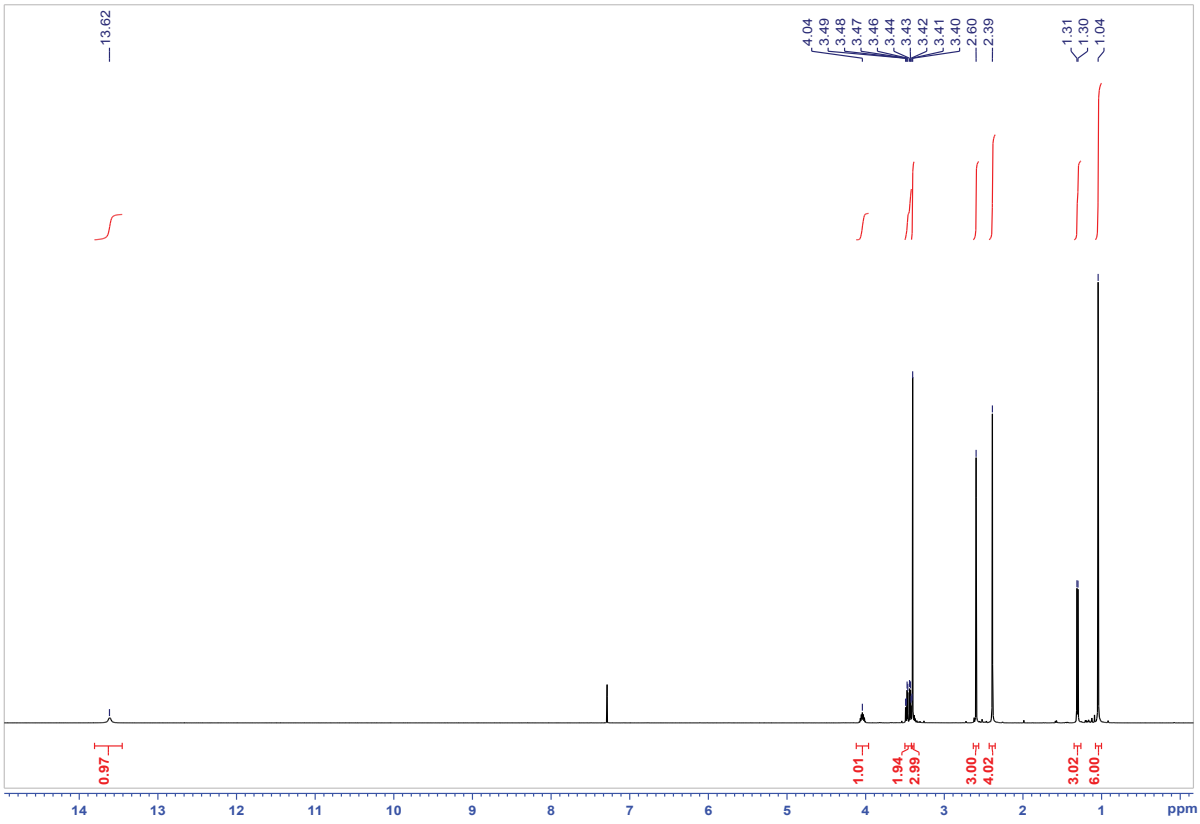

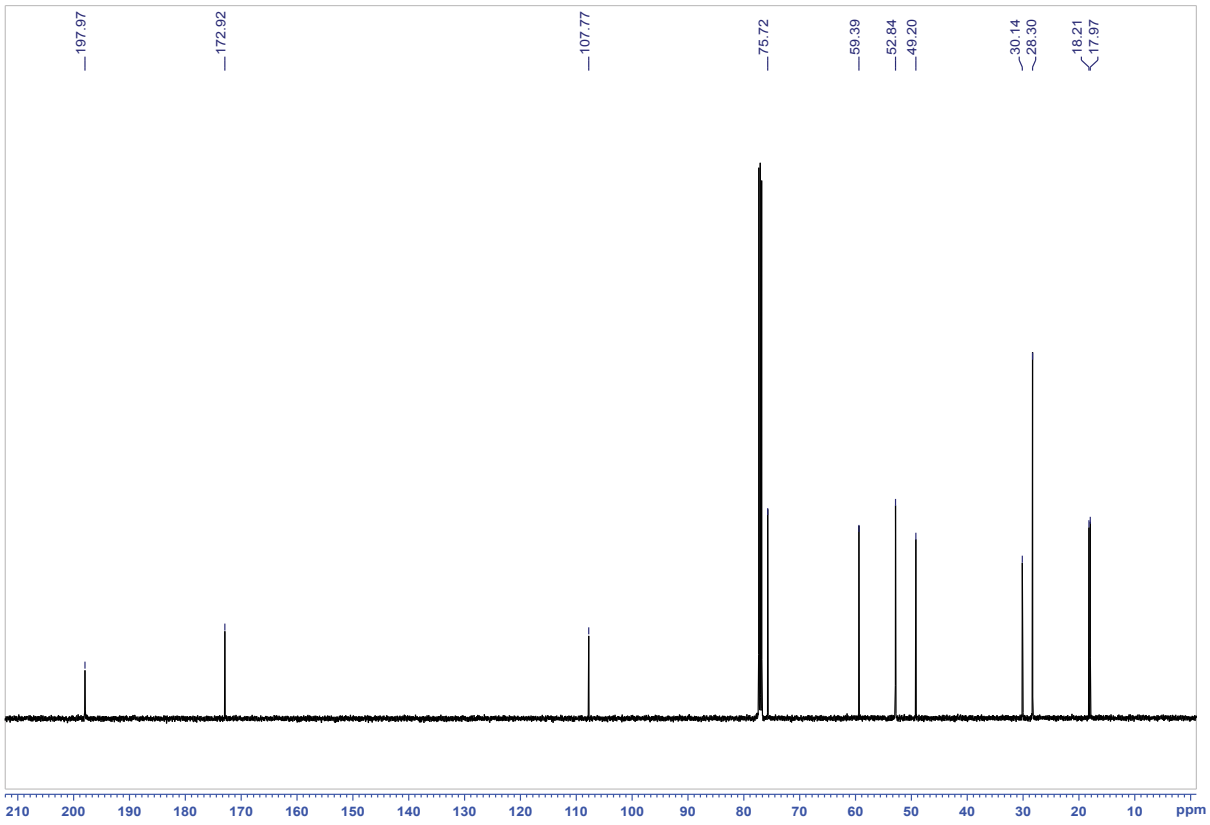
197.97
172.92
107.77
75.72
59.39
52.84
49.20
30.14
28.30
18.21
17.97
210 200 190 180 170 160 150 140 130 120 110 100 90 80 70 60 50 40 30 20 10 ppm

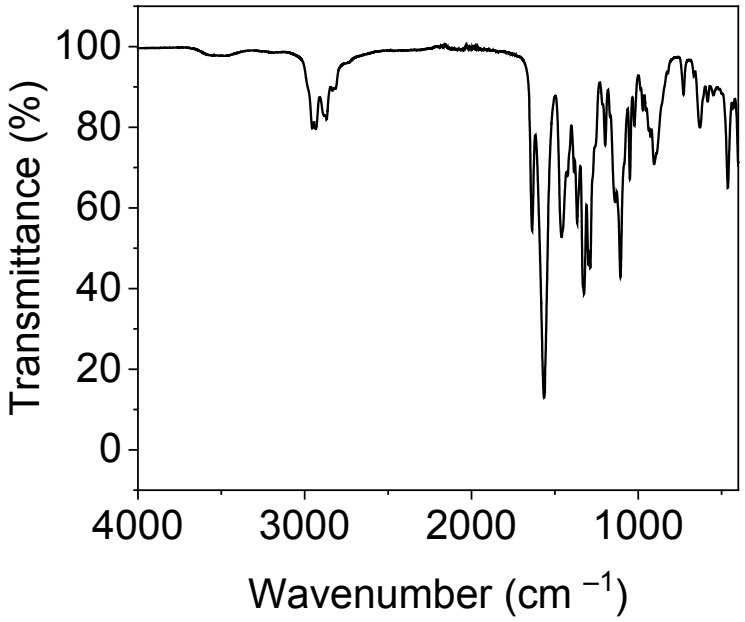
Transmittance (%)
100
80
60
40
20
0
4000
3000
2000
1000
Wavenumber (cm −1)

Characterization Methods

*Swelling measurement of PDK **1**–**3***

The swelling ratio measurement was carried out by an image-based method. PDK **1**–**3** was molded into 1 mm thick sheets and cut into 8 mm diameter round disks using a biopsy punch. The 8 mm disk was then clamped using an acid resistant tweezer and immersed into a 20 mL vial filled with acid solution (Fig. 1A inset picture). The vial was placed in an oil bath mounted on a hotplate for temperature control and the acid solution was gently stirred at 150 rpm. The tweezer that clamped the PDK disk was fixed during the swelling and deconstruction process and a fixed camera was used to take snapshots of the size of the PDK disk with set time intervals. The area of the PDK disk A_t at time t during deconstruction was extrapolated using Photoshop's selection and measurement tool. The areal swelling ratio was then determined by A_t / A_0, where A_0 is the initial PDK disk size. By assuming isotropic swelling of the PDK disc *(42)*, the volumetric swelling ratio V_t / V_0 was obtained by $(A_t / A_0)^{3/2}$.

*Kinetic Study of Acid-Catalyzed Hydrolytic Depolymerization of DKE **1**.*

The kinetic studies at 40 °C, 60 °C, 80 °C were carried out using the variable temperature preset in the NMR instrument. 5 mg of DKE **1** was dissolved in 650 µL of 5.0 M D_2SO_4/DCl/DBr solution and transferred in a sealed-cap NMR tube. The NMR tube was immediately mounted in the pre-heated NMR chamber and spectra were automatically acquired with a preset time interval. The degree of conversion was calculated using the integral ratio of signal at 2.36 ppm (m, 1H, –N*H*CH(CH_3)CH_2–) and the –CH_3 signal of the tail part of the DKE molecule. The procedure was repeated at different temperatures.

The pseudo first-order rate law:

$$\ln\left(\frac{[DKE]_t}{[DKE]_0}\right) = -k * t,$$

was used to calculate k at 40 °C, 60 °C, 80 °C for the three acids.

$\Delta G^{\ddagger}$ was calculated by fitting the values of k/T to $1000/T$ following the Eyring equation:

$$\ln\left(\frac{k}{T}\right) = \frac{-\Delta H^{\ddagger}}{RT} + \ln\left(\frac{k}{h}\right) + \frac{\Delta S^{\ddagger}}{R}$$

After extraction of $\Delta H^{\ddagger}$ and $\Delta S^{\ddagger}$, $\Delta G^{\ddagger}$ was calculated using $\Delta G^{\ddagger} = \Delta H^{\ddagger} - T\Delta S^{\ddagger}$

*Kinetic Study of Acid-Catalyzed Hydrolytic Depolymerization of PDK **1**.*

The kinetic studies at 60 °C were carried out using the in-situ NEXAFS techniques. The degree of deconstruction was monitored by observing the growing NEXAFS peak at 289.4 eV (**Fig. S11**). The pseudo first-order rate law:

$[Amine]_t = [Amine]_f\ (1 - e^{-kt})$,
was used to calculate *k* at 60 °C for the three acids. Where k is the rate constant to be extracted, t is the time elapsed for deconstruction, $[Amine]_f$ is the final concentration of amines at full deconstruction, and $[Amine]_t$ is the concentration of released amines at time t, which corresponds to the growing peak at 289.4 eV in **Fig. 2 C-E**.

Diffusion Ordered Spectroscopy (DOSY).
DKE **1** samples were placed in 5.0 M HBr or HCl solution in a 5 mm NMR tube with a concentration of 0.056 M to match MD simulation conditions. Self-diffusion coefficients were measured using pulsed field gradient (PFG) NMR at a field strength of 9.4 T on a Bruker NEO 400 MHz spectrometer fitted with a 5 mm water cooled double resonance broad band diffusion (diffBB) probe equipped with z-axis gradient and a variable temperature unit that was maintained at 25°C throughout measurements. A standard stimulated echo sequence (diffSTE) using sine-bell magnetic field gradient pulses was employed with application of eight dummy gradient pulses at the beginning of each program prior to spectral acquisition. Gradient strengths up to 100 G/cm in 16 equally spaced increments to achieve optimal signal attenuation were employed. All gradient pulse-pairs had a duration (δ) of 1 ms and diffusion time (Δ) of 20 ms. A repetition time of 5 s was used for all experiments.

The attenuation curve was fit to the Stejskal–Tanner equation:

$$\mathrm{S(g)} = \mathrm{S(0)exp}[-\mathrm{D} * \gamma^2 \mathrm{g}^2 \delta^2 \left(\Delta - \frac{\delta}{3}\right)]$$

where S(g) is the integrated signal at gradient strength g, D is the self-diffusion coefficient, and γ is the gyromagnetic ratio. Data was processed and analyzed in Bruker TopSpin 4.1 and Bruker Dynamics Center.

Theoretical Modeling and Methods

Time-Dependent Density Functional Theory (TD-DFT) Calculations.
TD-DFT calculations were performed within the Tamm–Dancoff approximation *(43)*, where the excitation energies (ω) and oscillator strengths are calculated as the solutions to the eigenvalue equation:

$$AX = \omega X \ldots (i)$$

The matrix **A** is given by:

$$A_{ai\sigma,bj\tau} = \delta_{ij}\delta_{ab}\delta_{\sigma\tau}(\epsilon_{a\sigma} - \epsilon_{a\tau}) + K_{ai\sigma,bj\tau} \ldots (ii)$$

In eqn. ***(ii)***, *i, j* and *a, b* denote occupied and virtual orbitals respectively, while σ and τ signify the spin indices. $\epsilon_{a\sigma}$ are the orbital energies in the unperturbed basis set and the linear response of the Kohn-Sham density matrix is captured in the matrix **X.** As observed in eqn. (iii), the coupling

matrix **K**, contains an exchange-correlation functional (E_{xc}) which needs to be accurately approximated for better agreement with experimental results.

$$K_{ai\sigma,bj\tau} = \left(\psi^*_{a\sigma}(r)\psi_{i\sigma}(r)\psi^*_{j\tau}(r)\psi_{b\tau}(r)\right) + \int dr\, dr'\ \psi^*_{a\sigma}(r)\psi_{i\sigma}(r)\frac{\delta^2 E_{XC}}{\delta\rho_\sigma(r)\delta\rho_\sigma(r')}\psi^*_{j\tau}(r)\psi_{b\tau}(r)\ldots(iii)$$

Determining the higher energy eigenvalues for the core-excitations necessitates the construction and subsequent diagonalization of the full matrix **A** which quickly becomes computationally prohibitive, especially for larger molecules. It is a common practice to restrict the TD-DFT calculation within the truncated space of single excitations from only the relevant core orbitals. Since the core orbitals are very well separated in terms of their energies from the other excluded orbitals, there is very little coupling between them, and previous works have demonstrated *(44)* negligible effects on the core excitation energies and oscillator strengths when the calculations are restricted to the single excitation space. In this work, only the excitations from the relevant C – 1s core orbitals in the three different small molecule representations (protonated DKE **1**, 2-Acetyl-5,5-dimethyl-1,3-cyclohexanedione, and 1-methoxy-2-propylamine) were considered.

The calculations were performed in QChem 5.4 *(45)*, and a specially designed short range corrected functional, SRC-R1 *(46)* was used with a 6-31+G* *(47)* basis set for approximating the exchange and correlation energies (E_{xc}). As the core-orbitals are significantly smaller in size, their integrals will be restricted to a small r and short-range corrected functionals like SRC-R1 introduce a fraction of exact Hartree-Fock exchange in the short-range to correct the systematic underestimation of excitation energies encountered in TD-DFT calculations with conventional DFT functionals.

A Full Width at Half Maximum (FWHM) of 0.25 was empirically chosen for constructing the gaussian distributions centered at the calculated excitation energies (ω) and the combined spectra was calculated for comparison with the experimental results. The computed spectra for the protonated DKE **1** have been compiled in the **Fig. S9** with the excitation energies and oscillator strengths of the major peaks in **Table S2**. The peak at slightly lower energy (286.174 eV) corresponds to the $C\ \sigma_{1s} \rightarrow\ C = N\ \pi^*$ virtual orbital while the other two peaks are for the $C\ \sigma_{1s} \rightarrow\ C = O\ \pi^*$ transitions. As seen in **Fig. S10**, change in the molecular conformation influences the calculated spectra. Therefore, all the TD-DFT calculations were preceded by a conformational search with CREST and the results from the lowest energy conformer was reported.

Classical Molecular Dynamics Simulation.

The classical molecular dynamics simulation was carried out in OpenMM (v. 7.7.0) *(48)* and the input script generation was facilitated by the pymatgen-io-openmm (v. 2023.7.14) class in pymatgen *(49)*. The Sage 0.2.0 *(50)* force field was used to describe the intermolecular forces among molecules in the system, with the pre-implemented water model TIP3P *(51)*. Sage force field uses Lennard-Jones (LJ) parameters validated in protein-ligand systems and the parameters were optimized against condensed phase mixture to describe nonbonded forces. The LJ cutoff distances for the simulations were chosen to be 0.9 nm. The partial charges were calculated with empirical MMFF94 *(52)* force field where the charges are generated based on the atom type, local

environment, aromatic ring and bond type. Periodic boundary conditions were imposed to the simulations to avoid edge effect on the surface atoms. 1 small protonated small molecule, 910 water, and 5M acids in the form of 91 anions (Cl^- /Br^- /I^-) and 90 hydronium ions are randomly packed by PACKMOL in a 25 × 25 × 25 (angstroms) boxes. The initial geometry is generated by pymatgen-io-openmm input generator with the PACKMOL random seed –1. All the acids are assumed to be fully dissociated as H_3O^+ and anions. All the charged species are charge-scaled by the factor 0.8, since the nonpolarizable force field used for the classical simulations are known to significantly overestimate ion pairing *(53)*.

The L-BFGS optimization algorithm was chosen for the energy minimization of the initial structures *(54)*. Given a Context specifying initial particle positions, it searches for a nearby set of positions that represent a local minimum of the potential energy. Distance constraints are enforced during minimization by adding a harmonic restraining force to the potential function. The strength of the restraining force is steadily increased until the minimum energy configuration satisfies all constraints to within the tolerance specified by the Context's Integrator. MD integrator type was LangevinMiddleIntegrator, which executes a Langevin dynamics, with the LFMiddle discretization *(55)*, where constraint tolerance = 1e–05, friction coefficient = 1 ps^{-1}, random seed = 0, step size = 0.001 ps, temperature = 298 K. The system was equilibrated with the NPT (MonteCarloBarostat) ensemble at 298 K and 1 atm for 1 ns and then subjected to a 3 ns annealing. Annealing started by increasing temperature to 400 K in 1 ns, followed by holding temperature at 400 K for 1 ns, and then decreasing temperature to 298 K in 1 ns. Finally, the annealed system was simulated with the NVT ensemble for 15 ns at 298 K to collect the production trajectory.

Convergence metrics.
To check the equilibration, potential energy, temperature, box volume and density change over time steps were plotted over the entire trajectory (0–19 ns). All of the metrics reached equilibrium before the production run (from 4 ns to 19 ns). The electrophile C–H_2O O RDF and N–H_2O O RDF plotted with the production data (around 15 ns in total) also showed that the simulation reached equilibrium during the production run.

Residence time calculation.
The residence time was calculated from the wrapped mode production trajectory where atoms move back from the other side of the simulation box rather than hanging out of the simulation box. The relevant atoms were selected by MDAnalysis *(56)* and the Residence class in SolvationAnalysis *(57)* were used for the calculation.
Residence time calculation method:
1. Create neighbor function (1 if coordinated, 0 otherwise) for each solute-solvent pair.
2. Calculate the auto covariance of neighbor function.
3. Average the resulting functions together to get the exponential.
4. Use fitting method or cutoff method to get the residence time where the autocovariance is small enough to be considered uncorrelated. For cutoff method, the residence time is the time frame x when the autocovariance is smaller than 1/e. For fitting method, the autocovariance curve is fitted by an exponential function (y = a*exp(–bx)+c)), then x = 1/b is taken as the residence time. The

real residence time is the time x * timestep of the simulation. In our calculation, we take the fitting method for higher accuracy (**Table S3**).

Hydrogen bond population calculation.

The hydrogen bond population was calculated from the wrapped mode production trajectory, by the HydrogenBondAnalysis class in MDAnalysis *(56)*. The distance cutoff used for finding donor-hydrogen pairs was 1.2 Å. The number of hydrogen bonds were averaged over all the time frames. Solvent hydrogen bond was calculated by counting hydrogen bond by type, averaging H–O···H type hydrogen bond numbers by time, and then normalizing the number by total number of water molecules including hydronium ions (**Table S4**). Solvent-DKE **1** iminium hydrogen bond was comprised of N–H···O and N···H type hydrogen bond (**Table S5**). The secondary amine N is very close to the electrophile C, which is also the reaction center.

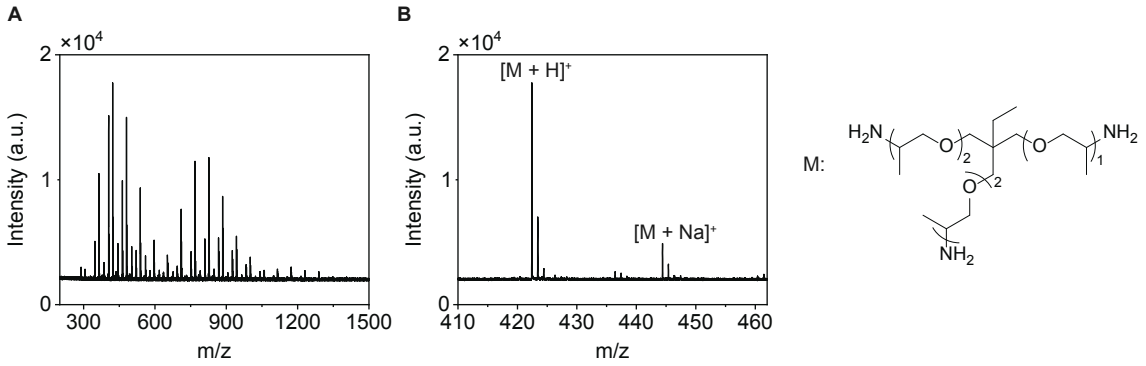

Fig. S1.
MALDI-ToF Spectrum of Triamine **1**. **(A)** MALDI-ToF spectrum of Triamine **1**. **(B)** Zoomed in MALDI-ToF spectrum of the highest peak and its expected chemical structure.

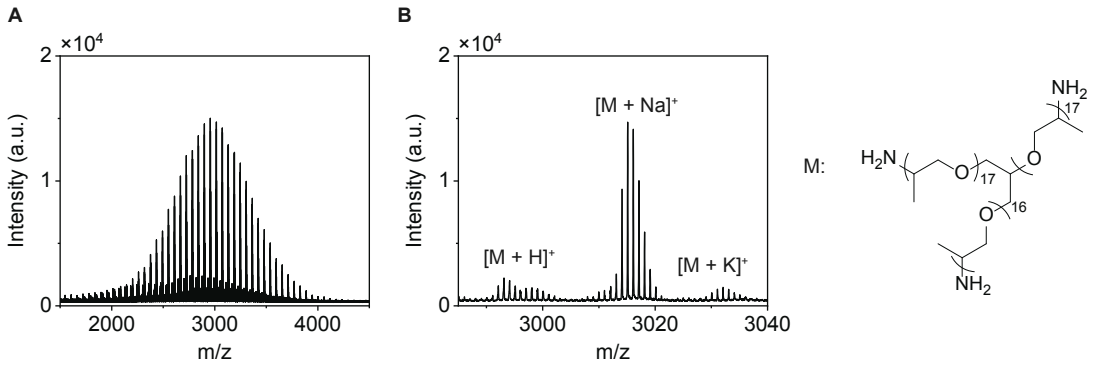

Fig. S2.
MALDI-ToF Spectrum of Triamine **2**. **(A)** MALDI-ToF spectrum of Triamine **2**. **(B)** Zoomed in MALDI-ToF spectrum of the highest peak and its expected chemical structure.

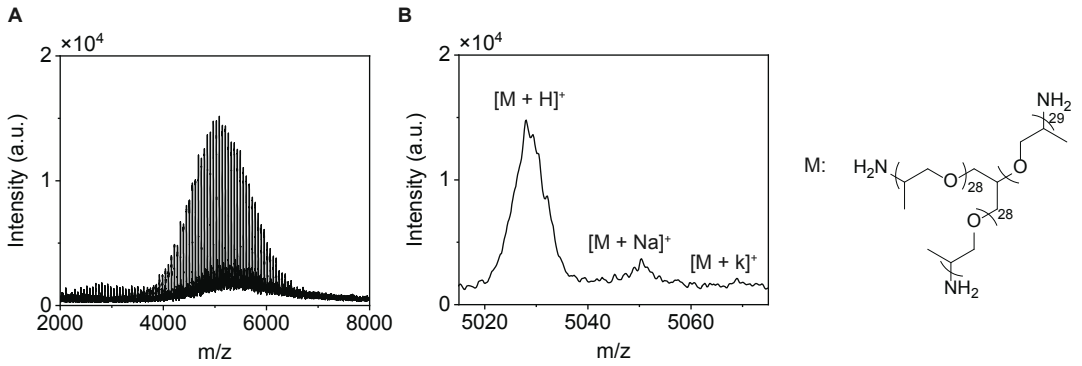

Fig. S3.
MALDI-ToF Spectrum of Triamine **3**. **(A)** MALDI-ToF spectrum of Triamine **3**. **(B)** Zoomed in MALDI-ToF spectrum of the highest peak and its expected chemical structure.

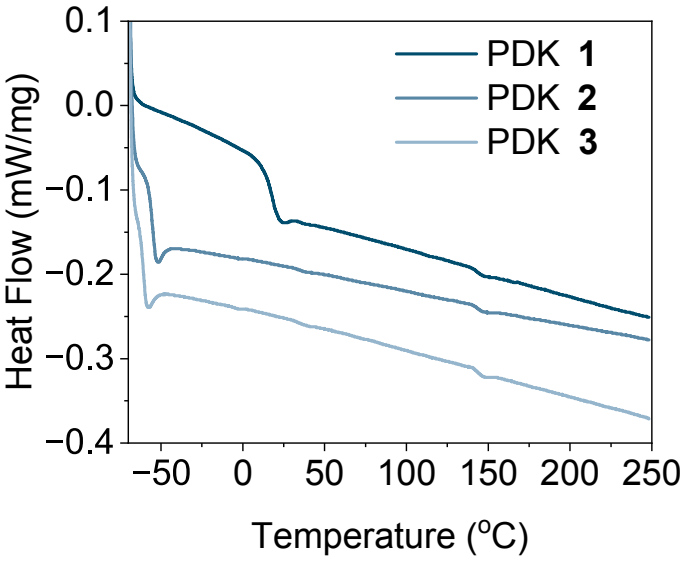

Fig. S4.
Differential Scanning Calorimetry (DSC) Plots of PDK elastomers **1**–**3**. PDK **1** showed T_g of 17 °C, PDK **2** showed T_g of –56 °C and PDK **3** showed T_g of –60 °C.

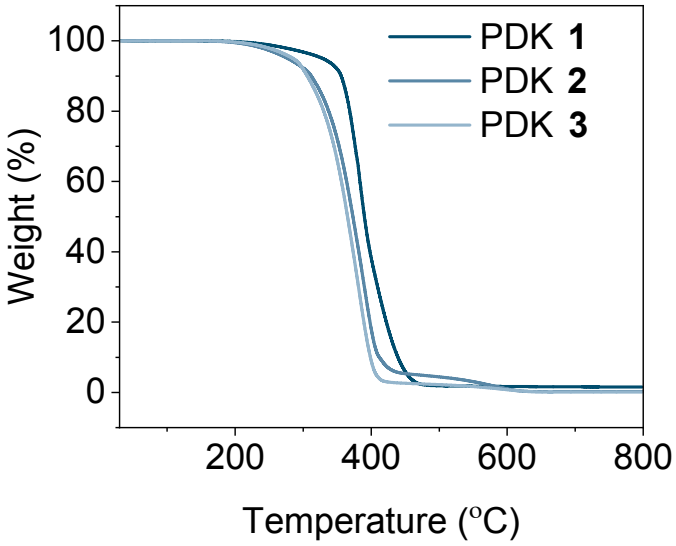

Fig. S5.
Thermal Gravimetric Analysis (TGA) Plots of PDK **1**–**3**. PDK **1** showed T_d (5% decomposition temperature) of 328 °C, PDK **2** showed T_d of 285 °C and PDK **3** showed T_d of 272 °C.

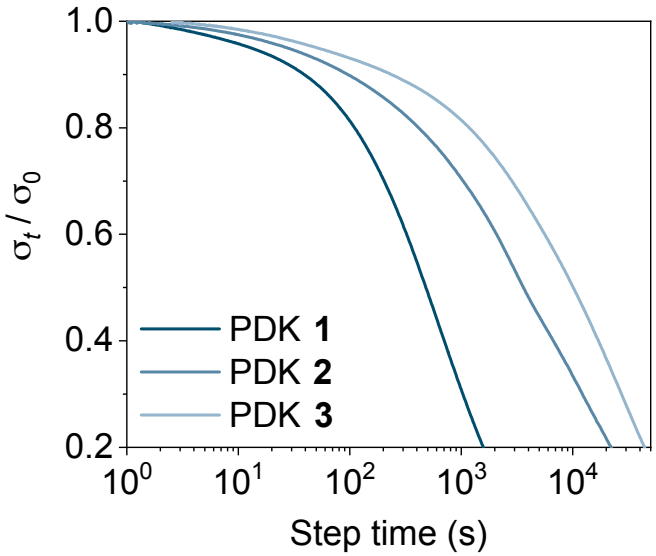

Fig. S6.
Stress Relaxation Plots of PDK elastomers **1**–**3**. PDK **1–3** undergo stress relaxation under 140 °C, indicating their ability to be thermally reprocessed to various shapes.

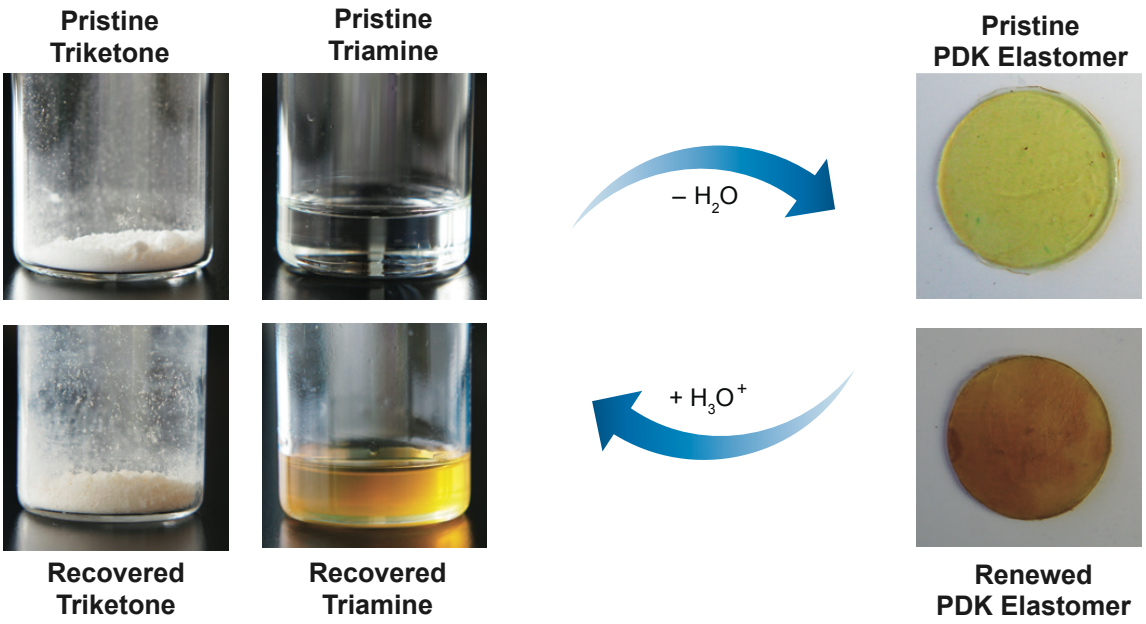

Fig. S7.
Pristine and Renewed PDK **1**. Pristine PDK **1** was first fabricated from pristine feedstocks and then deconstructed back to monomers. Renewed PDK **1** was fabricated from the recovered monomers collected from deconstructed pristine PDK **1**.

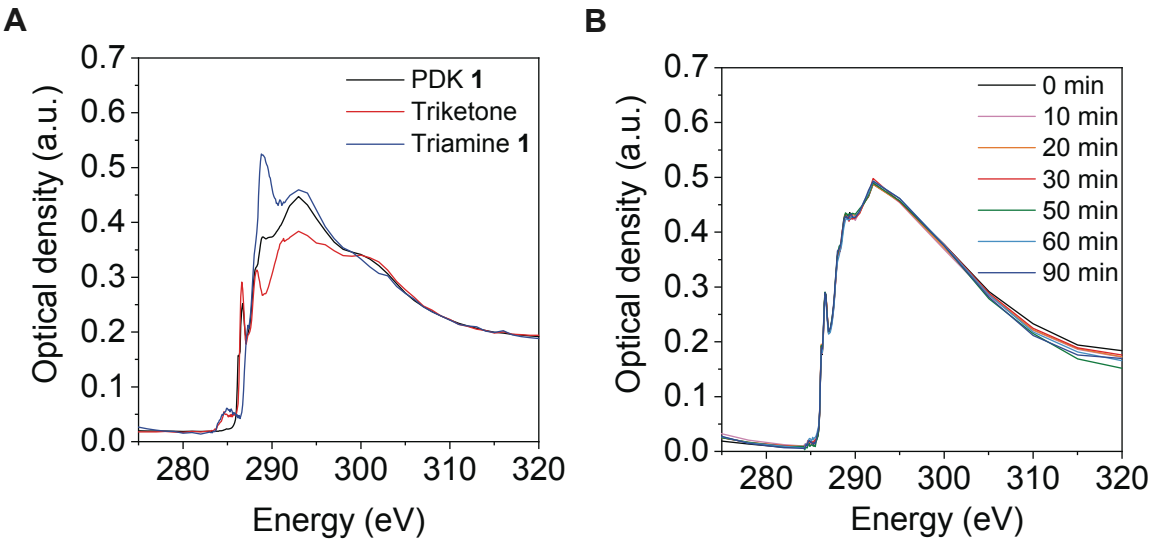

Fig. S8.
Assessing the extent of radiation damage. **(A)** NEXAFS spectra for pristine PDK **1**, TK **1** and triamine **1**. **(B)** The NEXAFS spectra of PDK **1** in 0.3 μL of deionized water during 90 min of irradiation with 320 eV X-ray at incidence flux that does not lead to noticeable radiation damage. The same incident X-ray flux was used for all other samples.

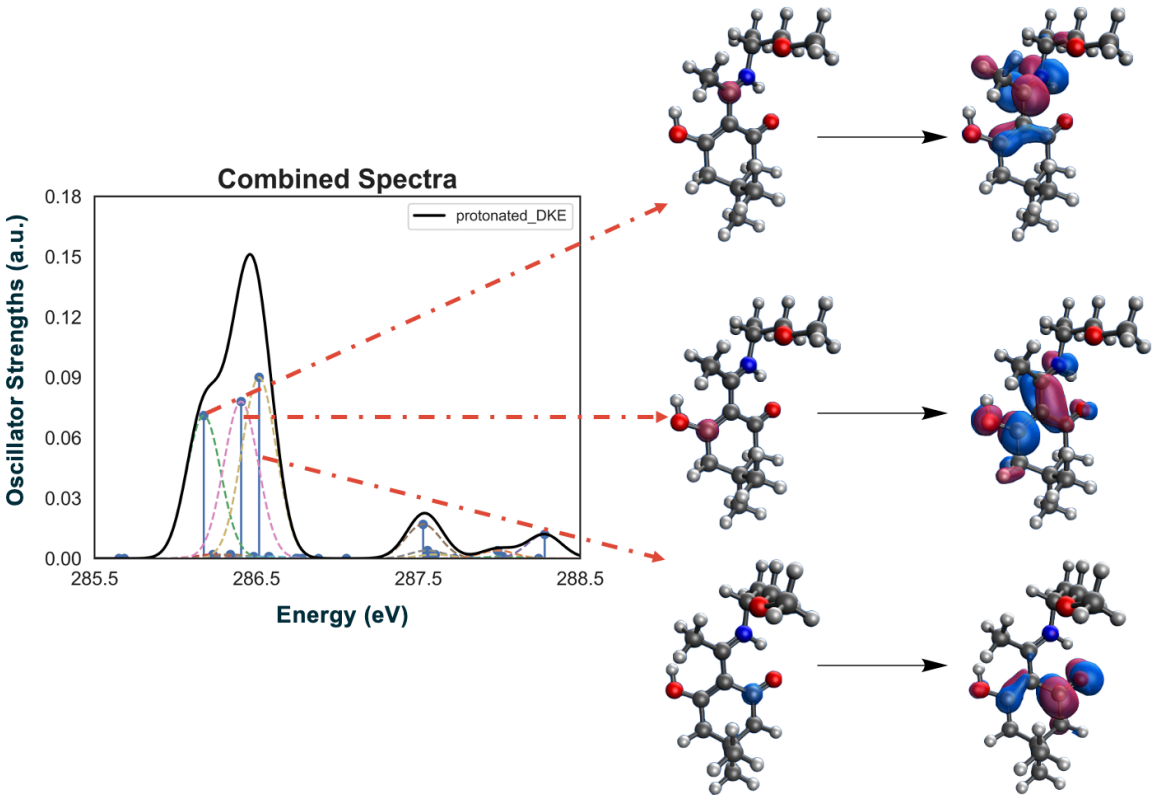

Fig. S9.
Individual Gaussians and the Calculated Combined Spectra for Protonated DKE **1**. The excited core orbital and the virtual orbitals where the electrons are excited to are also shown for the three major excitations. Atom colors: Carbon atom, dark gray; hydrogen atom, light gray; oxygen atom, red; nitrogen atom, blue.

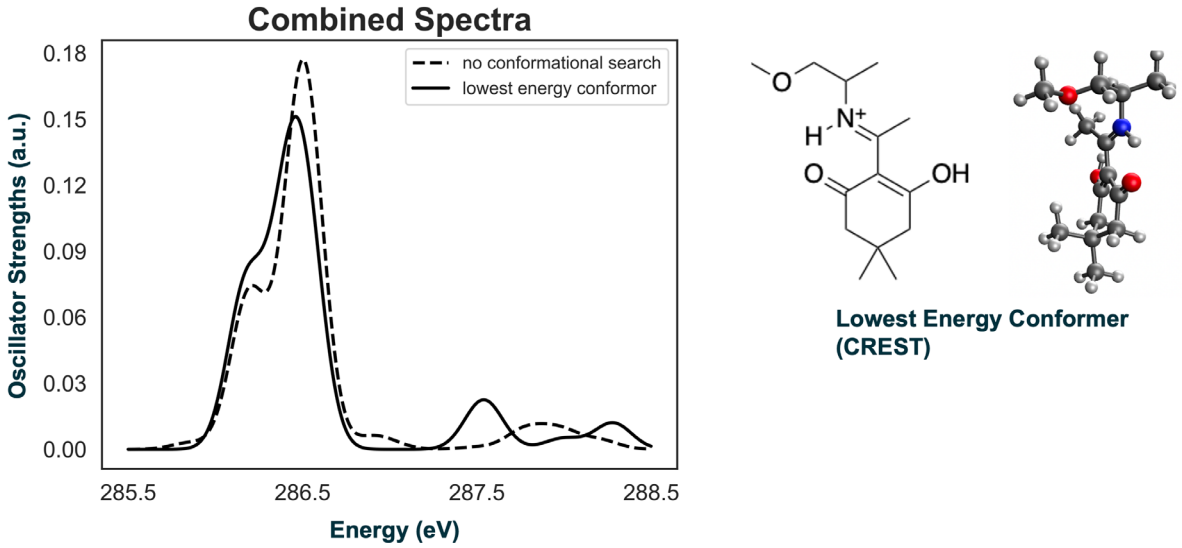

Fig. S10.
Effect of Conformations on the Calculated Combined Spectra for Protonated DKE **1**. The molecular structure of the CREST reported lowest energy conformer for the protonated DKE **1**. Atom colors: Carbon atom, dark gray; hydrogen atom, light gray; oxygen atom, red; nitrogen atom, blue.

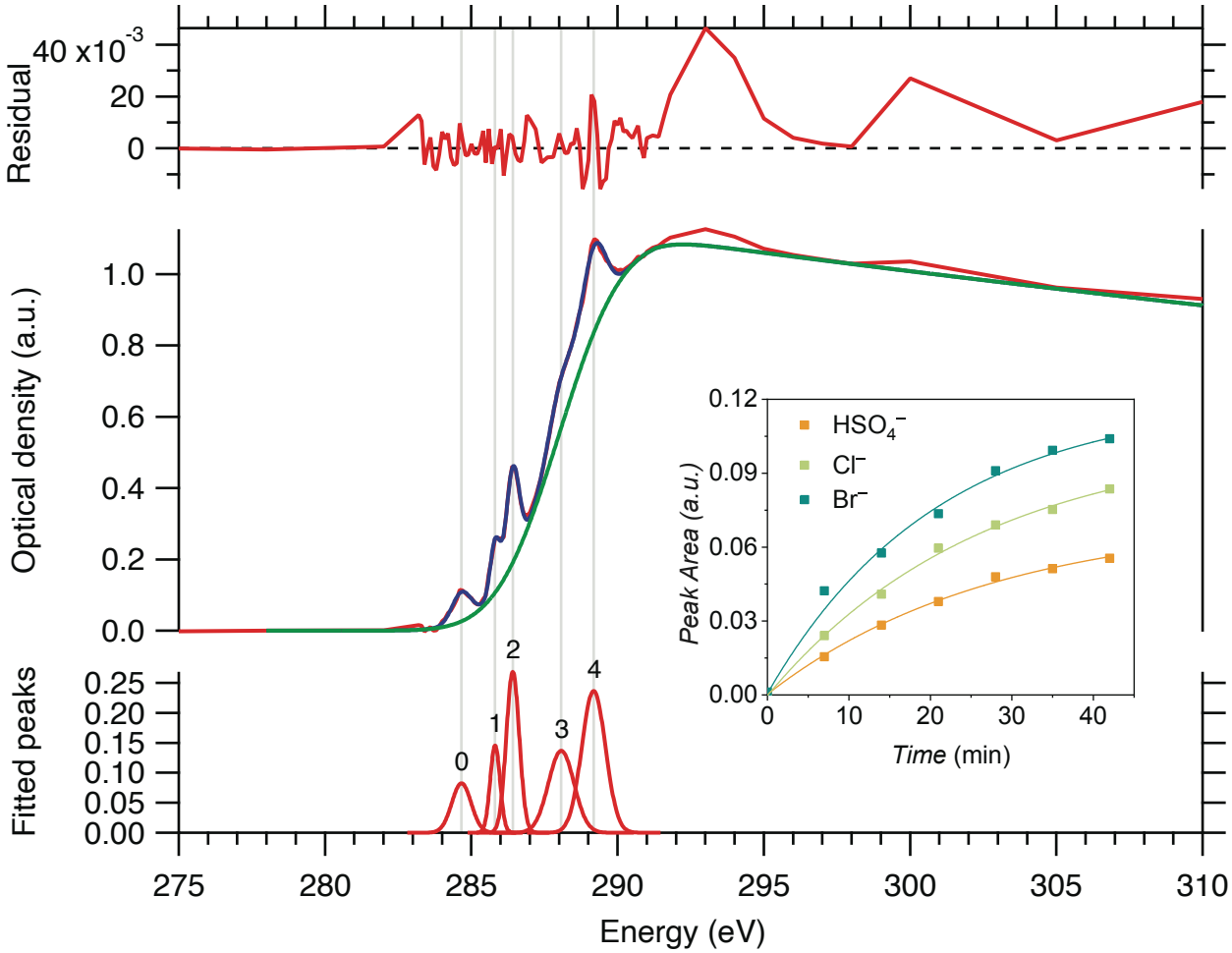

Fig. S11.
Peak fitting and rate extraction for the NEXAFS spectra of PDK **1**. Baselining and peak fitting of the NEXAFS spectrum. The inset shows the fitting of peak 4 areas to a pseudo-first-order kinetic model for the extraction of PDK **1** deconstruction rates. The adjusted R square values for the curve fitting are respectively 0.989, 0.993 and 0.988 for HSO_4^-, Cl^- and Br^-.

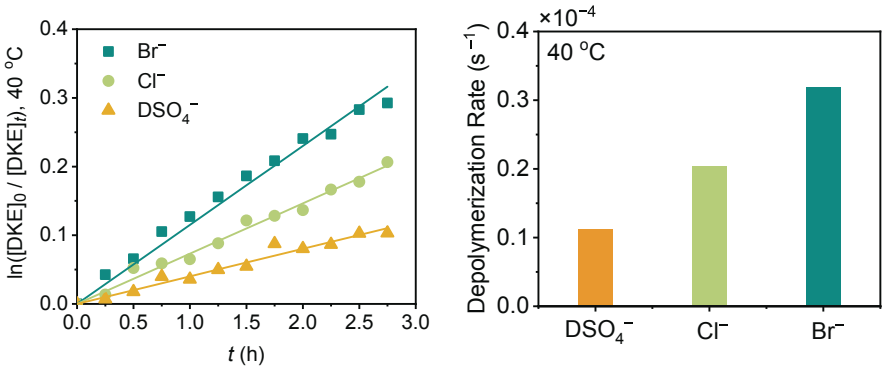

Fig. S12.
Kinetics of DKE **1** Acidolysis at 40 °C in 5.0 M D_2SO_4 / DCl / DBr.

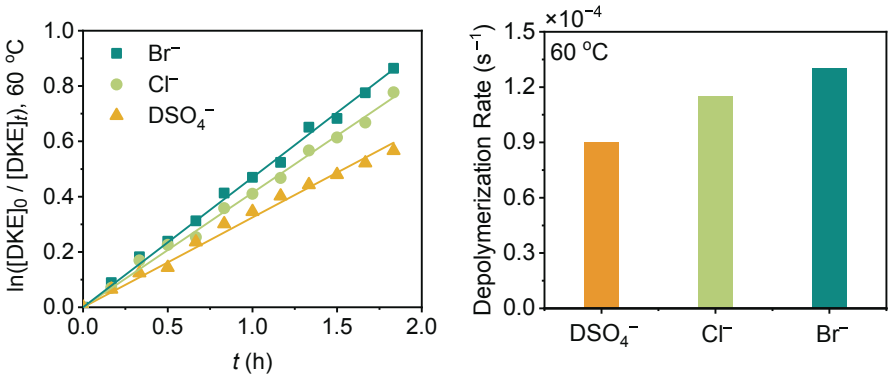

Fig. S13.
Kinetics of DKE **1** Acidolysis at 60 °C in 5.0 M D_2SO_4 / DCl / DBr.

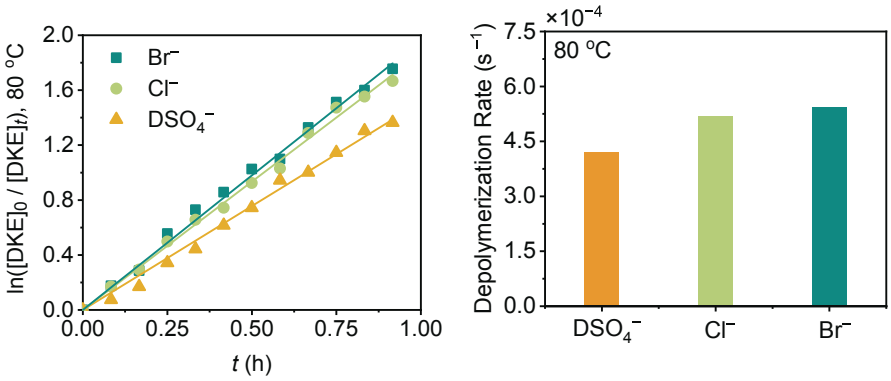

Fig. S14.
Kinetics of DKE **1** Acidolysis at 80 °C in 5.0 M D_2SO_4 / DCl / DBr.

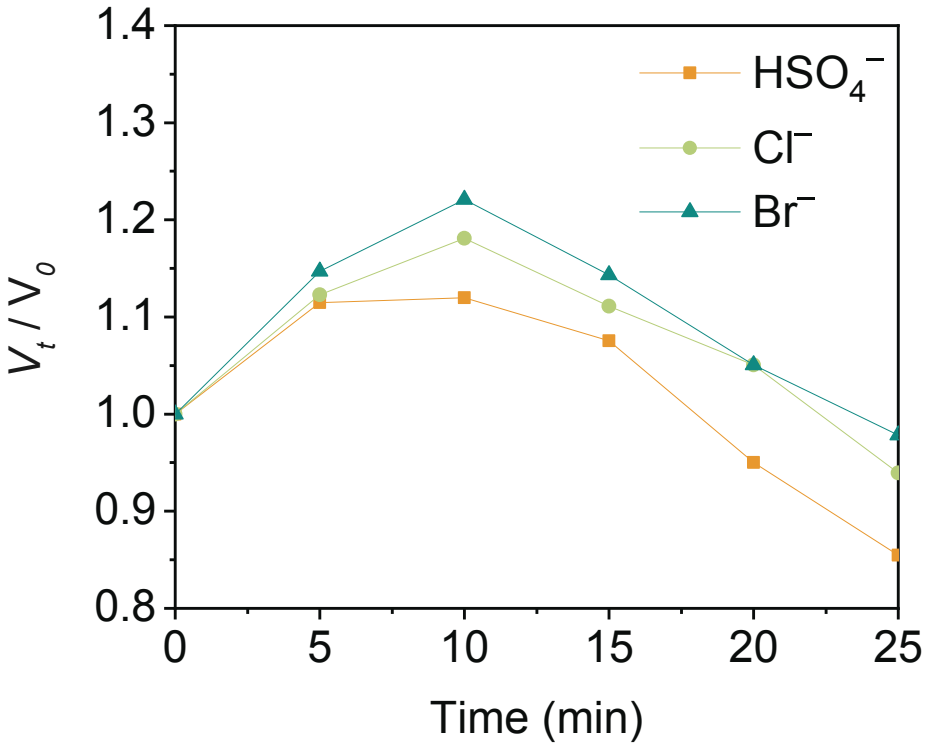

Fig. S15. Ratio of sample size at time t (V_t) over initial sample size (V_0) of PDK **1** at 60 °C in 5.0 M H_2SO_4 / HCl / HBr. The elastomer swells first and then become smaller in size as depolymerization takes place.

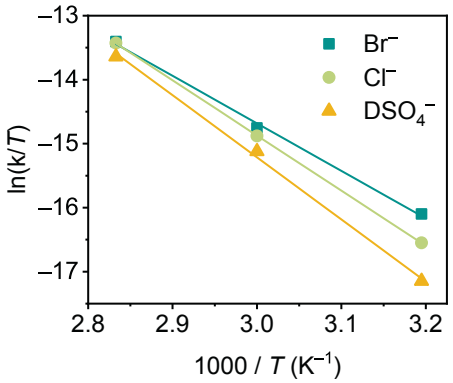

Fig. S16.
Eyring analysis of DKE **1** Acidolysis in 5.0 M D_2SO_4 / DCl / DBr.

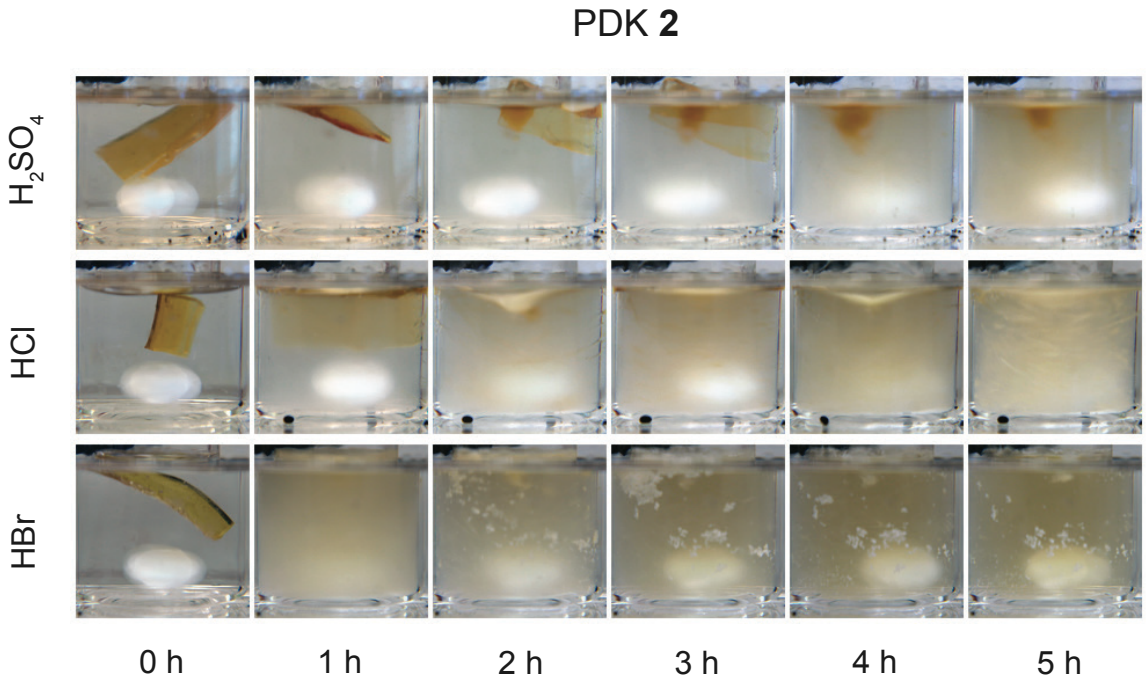

Fig. S17.
Depolymerization of PDK **2** in 5.0 M Acids. PDK **2** depolymerizing in 5.0 M H_2SO_4, 5.0 M HCl and 5.0 M HBr under 60 °C over the initial 5 h.

Fig. S18.
Depolymerization of PDK **1**. Depolymerized PDK **1** in 5.0 M H_2SO_4 (left), 5.0 M HCl (middle) and 5.0 M HBr (right). After stirring is stopped, the released triketone monomers would form precipitates that either float or sink depending on the density of the acid but is well separated from released triamine monomers that are dissolved in the aqueous phase.

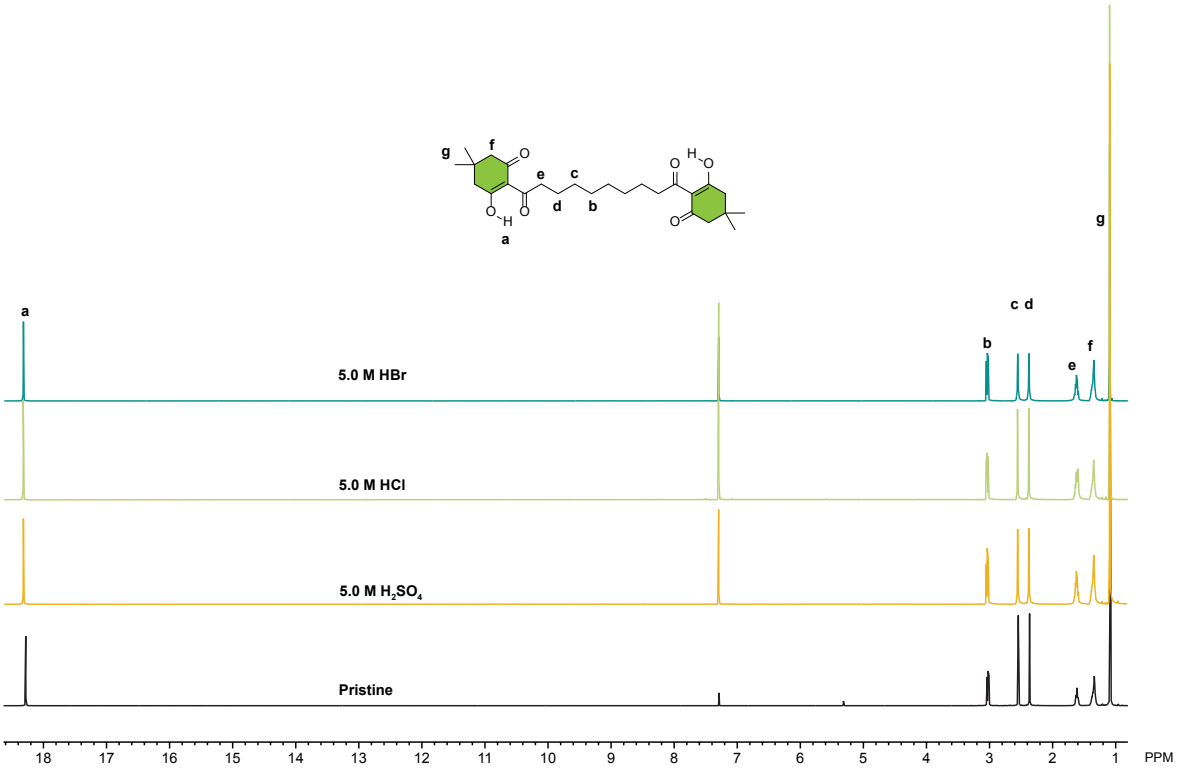

Fig. S19.
NMR Spectrum of Recovered Triketone TK **1** from PDK **1**.

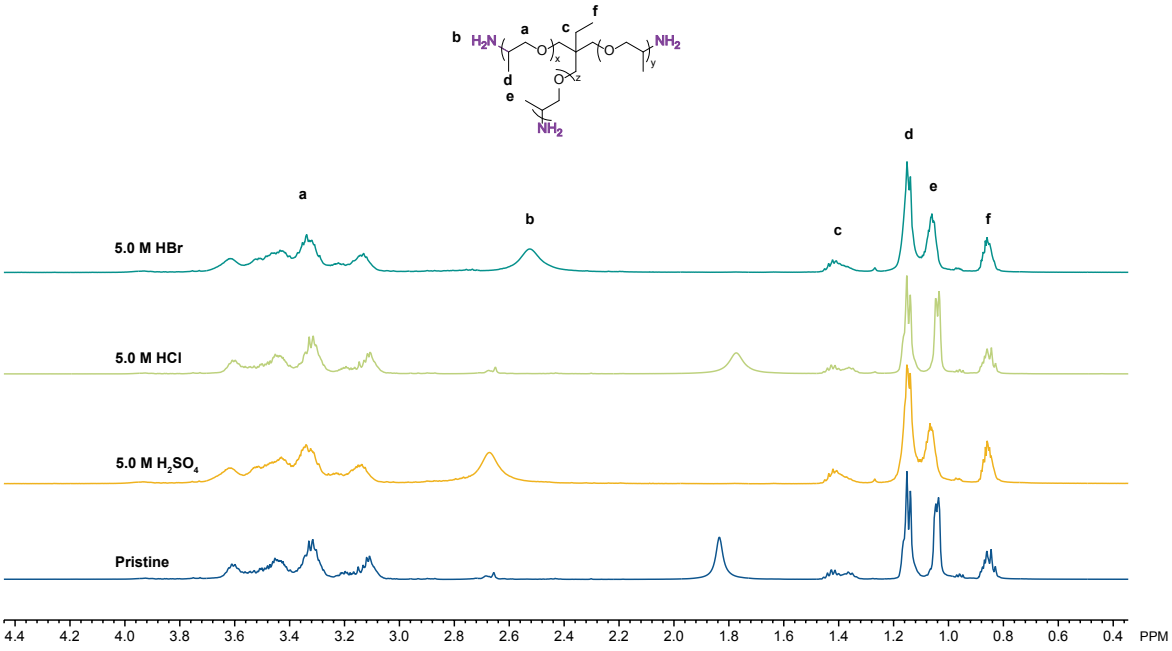

Fig. S20.
NMR Spectrum of Recovered Triamine **1** from PDK **1**.

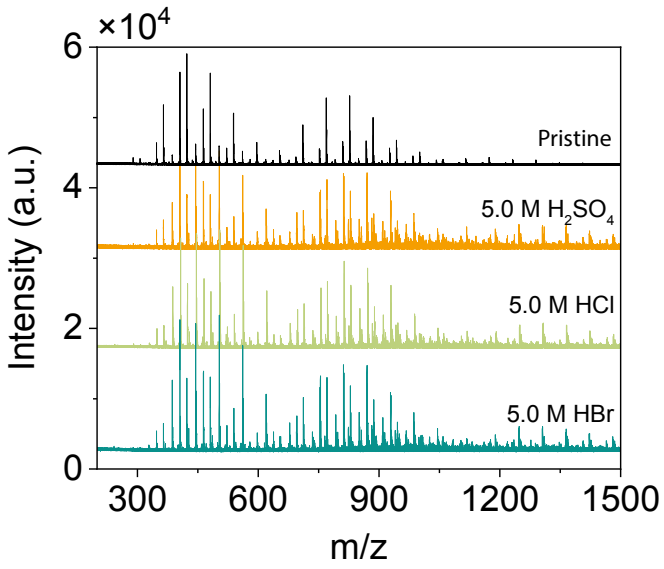

Fig. S21.
MALDI-ToF Spectrum of Pristine and Recovered Triamine **1** from PDK **1**.

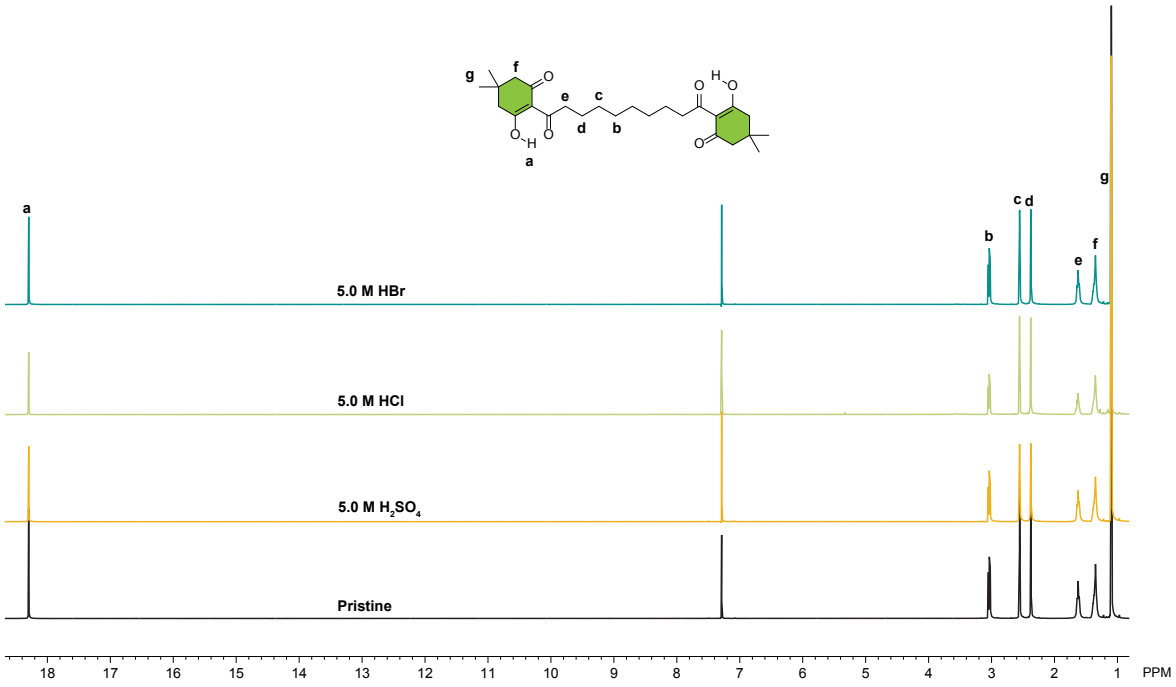

Fig. S22.
NMR Spectrum of Recovered Triketone TK **1** from PDK **2**.

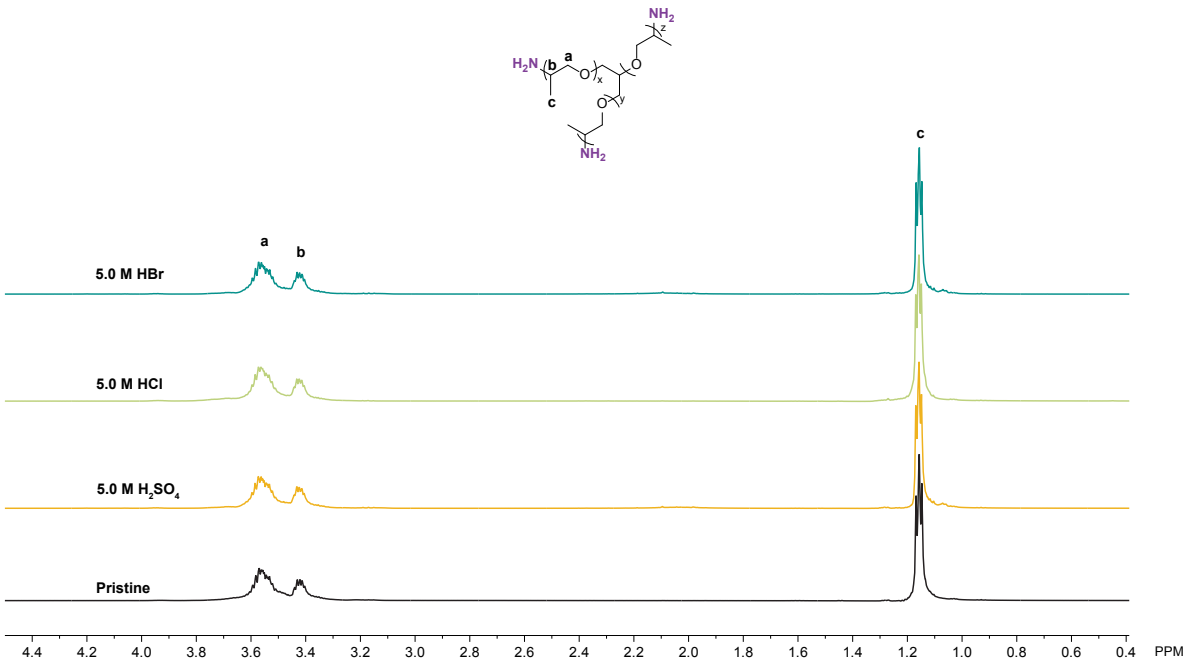

Fig. S23.
NMR Spectrum of Recovered Triamine **2** from PDK **2**.

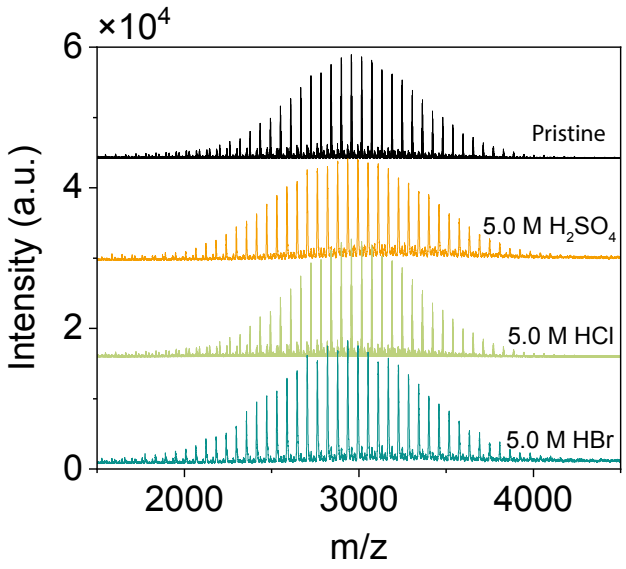

Fig. S24.
MALDI-ToF Spectrum of Pristine and Recovered Triamine **2** from PDK **2**.

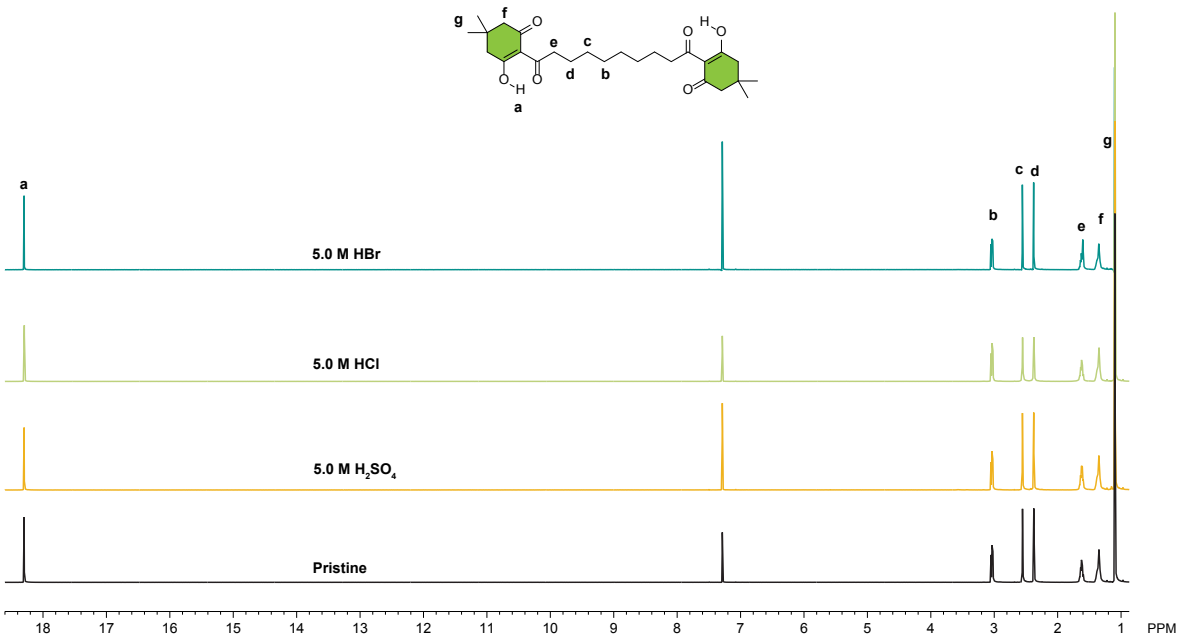

Fig. S25.
NMR Spectrum of Recovered Triketone TK **1** from PDK **3**.

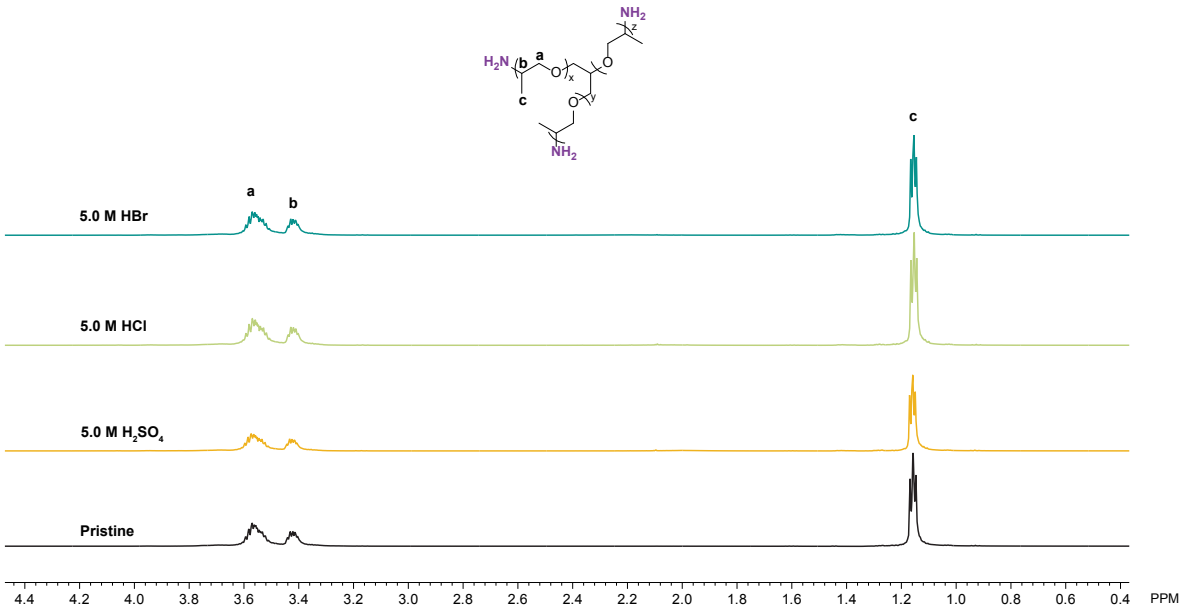

Fig. S26.
NMR Spectrum of Recovered Triamine **3** from PDK **3**.

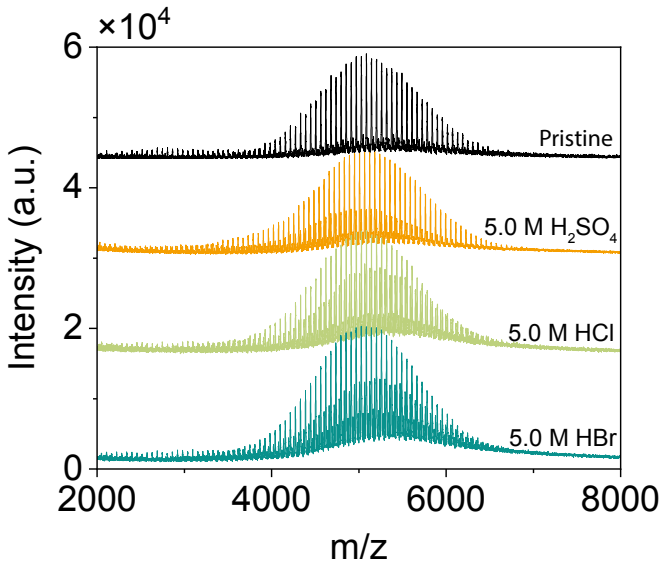

Fig. S27.
MALDI-ToF Spectrum of Pristine and Recovered Triamine **3** from PDK **3**.

Table S1 Diffusion Ordered Spectroscopy of DKE **1** in 5.0 M Acids

	Diffusivity of H_3O^+ (10^{-9} m^2s^{-1})	Diffusivity of DKE **1** (10^{-9} m^2s^{-1})
5.0 M HCl	1.47	0.37
5.0 M HBr	1.51	0.385

Table S2 Excitation energies and oscillator strengths for the three major peaks in DKE **1** as plotted in Fig. **S9**

Peak position (eV)	**Strength**
286.174	0.071
286.405	0.078
286.516	0.090

Table S3 Electrophile C–H_2O Residence Time (ps) in Various 5.0 M Acids by MD simulation

5.0 M HCl	5.0 M HBr	5.0 M HI
28.2	29.8	34.8

Table S4 Hydrogen Bond among solvent molecules in Various 5.0 M Acids by MD simulation

	Solvent H–O···H
5.0 M HCl	0.565
5.0 M HBr	0.541
5.0 M HI	0.526

Table S5 Hydrogen Bond around N Atom in Various 5.0 M Acids by MD simulation

	N–H···O	N···H
5.0 M HCl	0.457	0.003
5.0 M HBr	0.490	0.013
5.0 M HI	0.533	0.003